



# Laser-Raman Measurements in the Muzzle Blast Region of a 20-mm Cannon

W. D. Williams and H. M. Powell  
ARO, Inc.

August 1980

Final Report for Period October 1978 — September 1979

Approved for public release; distribution unlimited.

**ARNOLD ENGINEERING DEVELOPMENT CENTER  
ARNOLD AIR FORCE STATION, TENNESSEE  
AIR FORCE SYSTEMS COMMAND  
UNITED STATES AIR FORCE**

## NOTICES

When U. S. Government drawings, specifications, or other data are used for any purpose other than a definitely related Government procurement operation, the Government thereby incurs no responsibility nor any obligation whatsoever, and the fact that the Government may have formulated, furnished, or in any way supplied the said drawings, specifications, or other data, is not to be regarded by implication or otherwise, or in any manner licensing the holder or any other person or corporation, or conveying any rights or permission to manufacture, use, or sell any patented invention that may in any way be related thereto.

Qualified users may obtain copies of this report from the Defense Technical Information Center.

References to named commercial products in this report are not to be considered in any sense as an indorsement of the product by the United States Air Force or the Government.

This report has been reviewed by the Office of Public Affairs (PA) and is releasable to the National Technical Information Service (NTIS). At NTIS, it will be available to the general public, including foreign nations.

## APPROVAL STATEMENT

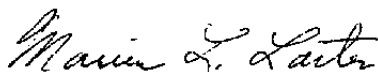
This report has been reviewed and approved.



KENNETH H. LENERS, Captain, USAF  
Project Manager  
Directorate of Technology

Approved for publication:

FOR THE COMMANDER



MARION L. LASTER  
Director of Technology  
Deputy for Operations

# UNCLASSIFIED

REPORT DOCUMENTATION PAGE		READ INSTRUCTIONS BEFORE COMPLETING FORM
1. REPORT NUMBER AEDC-TR-79-72	2. GOVT ACCESSION NO.	3. RECIPIENT'S CATALOG NUMBER
4. TITLE (and Subtitle) LASER-RAMAN MEASUREMENTS IN THE MUZZLE BLAST REGION OF A 20-MM CANNON		5. TYPE OF REPORT & PERIOD COVERED Final Report, October 1978 - September 1979
		6. PERFORMING ORG. REPORT NUMBER
7. AUTHOR(s) W. D. Williams and H. M. Powell, ARO, Inc., a Sverdrup Corporation Company		8. CONTRACT OR GRANT NUMBER(s)
9. PERFORMING ORGANIZATION NAME AND ADDRESS Arnold Engineering Development Center/DOT Air Force Systems Command Arnold Air Force Station, TN 37389		10. PROGRAM ELEMENT, PROJECT, TASK AREA & WORK UNIT NUMBERS Program Element 921C10
11. CONTROLLING OFFICE NAME AND ADDRESS Arnold Engineering Development Center/DOS Air Force Systems Command Arnold Air Force Station, TN 37389		12. REPORT DATE August 1980
		13. NUMBER OF PAGES 43
14. MONITORING AGENCY NAME & ADDRESS (if different from Controlling Office)		15. SECURITY CLASS. (of this report)  UNCLASSIFIED
		15a. DECLASSIFICATION/DOWNGRADING SCHEDULE N/A
16. DISTRIBUTION STATEMENT (of this Report)  Approved for public release; distribution unlimited.		
17. DISTRIBUTION STATEMENT (of the abstract entered in Block 20, if different from Report)		
18. SUPPLEMENTARY NOTES  Available in the Defense Technical Information Center (DTIC).		
19. KEY WORDS (Continue on reverse side if necessary and identify by block number) antiaircraft guns                      emission                                      Raman spectra gas dynamics                              propellant flashes blast    laser beams gun barrels                                      light scattering		
20. ABSTRACT (Continue on reverse side if necessary and identify by block number) Laser-Raman diagnostics have been used to determine the temporal variation of N <sub>2</sub> and CO number densities in the muzzle blast region of a 20-mm Vulcan cannon. The measurements were made within 3.18 to 13.0 mm of the muzzle exit plane on the cannon axial centerline. Propellant WC-870 was used, and the rounds were downloaded to give a muzzle exit velocity of ≈ 470 m/sec. A standard 98-gram projectile was launched.		

# UNCLASSIFIED

## PREFACE

The work reported herein was conducted by the Arnold Engineering Development Center (AEDC), Air Force Systems Command (AFSC), at the request of the U. S. Army Ballistic Research Laboratory (BRL). The results of the research were obtained by ARO, Inc., AEDC Division (a Sverdrup Corporation Company), operating contractor for the AEDC, AFSC, Arnold Air Force Station, Tennessee, under ARO Project Number P34M-21A. The AEDC project manager was Capt. Kenneth H. Leners. The data analysis was completed on July 15, 1979, and the manuscript was submitted for publication on September 19, 1979.

## CONTENTS

	<u>Page</u>
1.0 INTRODUCTION .....	5
1.1 Overall Objectives .....	5
1.2 Specific Objectives .....	5
1.3 Description of the Flow Field .....	6
2.0 EXPERIMENTAL SETUP AND OPERATION .....	9
2.1 Cannon and Diaphragm Test Room Arrangement .....	9
2.2 Laser System .....	12
2.3 Spectrometer System .....	13
2.4 Data Acquisition System .....	13
3.0 LASER-RAMAN MEASUREMENT TECHNIQUE .....	20
3.1 Spectra and Intensity Relations .....	20
3.2 Calibrations .....	32
3.3 Data Reduction .....	33
4.0 DISCUSSION .....	34
4.1 Chronology of Experiments .....	34
4.2 Raman Results and Comparisons with Predictions .....	37
4.3 Results from Laser-Induced Incandescence .....	38
5.0 SUMMARY .....	38
5.1 Conclusions .....	38
5.2 Future Work .....	39
REFERENCES .....	40

## ILLUSTRATIONS

### Figure

1. Muzzle Exit Temperature as a Function of Muzzle Velocity .....	6
2. Precursor Flow Regime, $t < 0$ .....	7
3. Propellant Gas Flow Regime, $t \geq 0$ .....	8
4. Estimate of Exit Plane Flow Properties .....	9
5. Experimental Arrangement, View No. 1 .....	10
6. Experimental Arrangement, View No. 2 .....	10
7. Experimental Arrangement, View No. 3 .....	11
8. Projectile Catcher Assembly .....	12
9. Block Diagram of System Setup for Cannon Firing and Synchronization .....	15

<u>Figure</u>	<u>Page</u>
10. Timing Diagram for Major Control Events .....	16
11. Typical Transducer Waveforms Used for Velocity Measurements .....	17
12. Block Diagram of the Electronic System Applicable During the Data Acquisition Interval; Q-Switch Mode/Integrator .....	18
13. Timing Diagram for Data Acquisition Interval .....	19
14. Block Diagram of the Electronic System Applicable During the Data Acquisition Interval; Conventional Mode/Integrator .....	21
15. Block Diagram of the Electronic System Applicable During the Data Acquisition Interval; Conventional Mode/Photon Counting .....	22
16. N <sub>2</sub> and CO Vibration-Rotation Bands at T = 300 K .....	25
17. N <sub>2</sub> and CO Vibration-Rotation Bands at T = 700 K .....	26
18. N <sub>2</sub> and CO Vibration-Rotation Bands at T = 1,100 K .....	27
19. Calculated Intensity Ratio, R <sub>v</sub> , and Temperature-Dependent Correction Factors, C <sub>F</sub> (T,X), as a Function of Temperature .....	28
20. N <sub>2</sub> , CO, and CO <sub>2</sub> Rotational Raman Structure, T = 300 K .....	29
21. N <sub>2</sub> , CO, and CO <sub>2</sub> Rotational Raman Structure, T = 700 K .....	30
22. N <sub>2</sub> , CO, and CO <sub>2</sub> Rotational Raman Structure, T = 1,100 K .....	31
23. Calculated Intensity Ratio, R <sub>R</sub> , as a Function of Temperature .....	32
24. Fractional Laser Beam Transmission as a Function of Time .....	34
25. Laser Power Density at Focal Volume, watts/cm <sup>2</sup> .....	36
26. Measured Relative Number Densities as a Function of Time .....	37

### TABLES

1. Predicted Species Mole Fractions for Propellant Gas .....	8
2. Nominal Wavelengths for Vibration-Rotation Stokes Bands of Propellant Gas Species for a Laser Excitation Wavelength of 6,943 Å .....	23
 NOMENCLATURE .....	 42

## 1.0 INTRODUCTION

### 1.1 OVERALL OBJECTIVES

Quantitative studies of muzzle blast flow fields have been under way at the U. S. Army Ballistic Research Laboratory (BRL) since 1973 (Refs. 1 through 4). These studies have been conducted because of interest in the effects of the muzzle blast on both finned and unfinned projectile trajectories and the environmental signature of the muzzle blast. Static temperature is a muzzle blast flow-field property of particular importance. The development of the muzzle blast has been shown (Refs. 2 and 5) to follow predictions from spherical, strong blast theory (Ref. 6) on the basis of the initial rate of energy efflux from the muzzle. Gas temperature has a significant influence upon the initial rate of energy efflux (Ref. 3). Unfortunately, there is considerable disagreement between the theoretical predictions of temperature from Refs. 7 and 8, and both theories disagree with the acoustic measurements of temperature from Ref. 3 and the infrared spectroscopic measurements of Ref. 9. The state of disagreement is shown in Fig. 1, which was taken from Ref. 3. The overall objectives of the present experiments were 1) to provide information about the muzzle blast region that could resolve the dilemma depicted in Fig. 1, and 2) to verify the applicability of laser-Raman diagnostics for short-pulse expansions.

Areas of interest directly related to the laser-Raman muzzle blast effort included:

- a. The applicability of laser-Raman diagnostics for solid rocket engine exhausts which have similarities with the muzzle blast environment in both 1) temporal requirements and 2) gas species and particulate constituency.
- b. The study of the interaction of the muzzle exhaust of repetitive, rapid-firing weapons and air-breathing aircraft engines.

### 1.2 SPECIFIC OBJECTIVES

The specific objectives were to determine the time history of static temperature on the axial centerline of the muzzle blast region as near to the muzzle exit plane as possible and to measure the species densities or relative species densities at the same time and axial position at which temperatures were obtained.

The laser-Raman diagnostic technique was used to perform these measurements. A Q-switch or conventional mode pulsed ruby laser provided excitation, and a double-grating spectrometer provided spectral selection. A dual photomultiplier tube arrangement was used to permit measurement of either rotational or vibrational temperature, from which static temperature could be inferred.

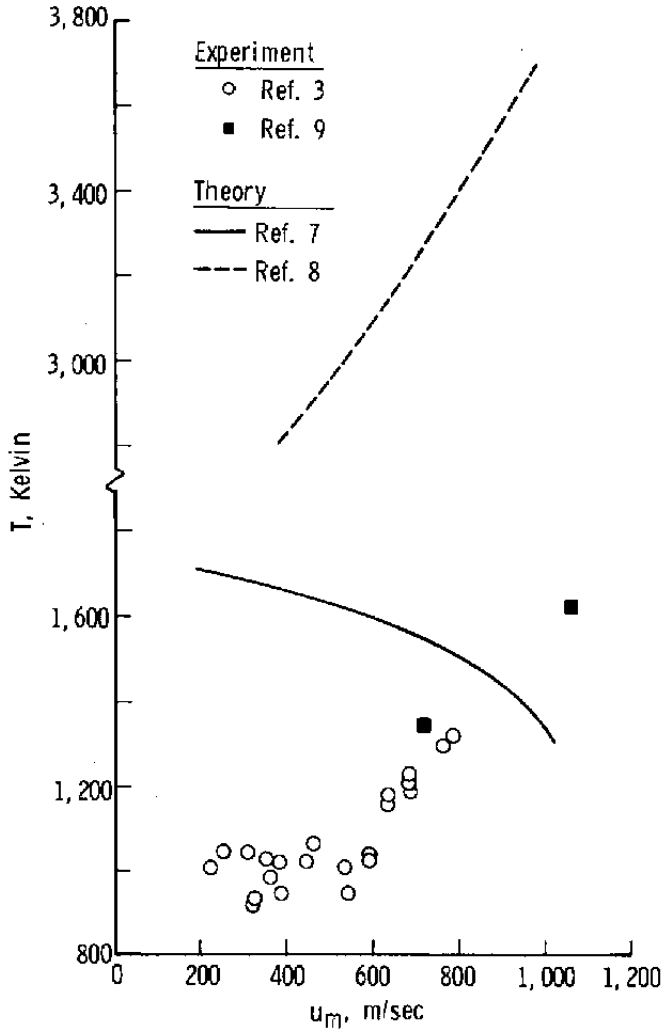


Figure 1. Muzzle exit temperature as a function of muzzle velocity.

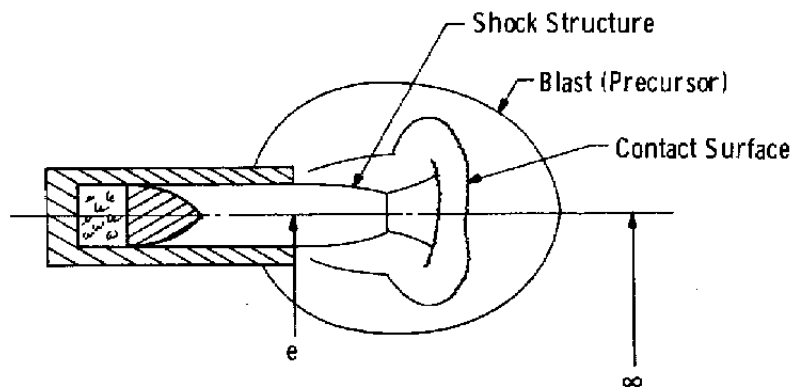
### 1.3 DESCRIPTION OF THE FLOW FIELD

The muzzle flow field is described in detail in Refs. 1 through 3; therefore, only a brief description need be given here. The muzzle flow may be divided into two parts, the precursor flow and the propellant gas flow. The precursor flow regime exists before the



projectile exits the muzzle ( $t < 0$ ), and the flow is formed as the tube gases are expelled from the cannon bore by the projectile. These gases are composed of air and any residual and leaked propellant gases.

Compression waves move ahead of the accelerating projectile and coalesce to form a shock wave. To obtain an adequate prediction of exit static pressure ( $p_e$ ), exit Mach number ( $M_e$ ), and exit shock velocity, the Rankine-Hugoniot relations can be used on the assumption that the gas velocity is equal to the projectile launch velocity (Ref. 10). For high-speed projectiles the major acceleration occurs near the breech, and the projectile velocity is relatively constant over the in-bore trajectory. The precursor flow regime is depicted schematically in Fig. 2, and for a projectile launch velocity of 470 m/sec a static temperature of 528 K and a nitrogen number density of  $5.23 \times 10^{19}/\text{cm}^3$  is predicted near the muzzle exit.



$$\begin{aligned} \gamma_e &= 1.4 \text{ (Air)}, u_e = u_m = 470 \text{ m/sec} \\ M_e &= 1.02 \\ \frac{p_e}{p_\infty} &= 5.027, \frac{T_e}{T_\infty} = 1.779 \\ n_e(\text{N}_2) &= 5.23 \times 10^{19} \text{ cm}^{-3} \\ p_\infty &= 730 \text{ torr}, T_\infty = 297 \text{ K} \end{aligned}$$

Figure 2. Precursor flow regime,  $t < 0$ .

Whenever the projectile base clears the muzzle exit ( $t = 0$ ), the propellant flow regime begins. As noted in Ref. 3, the high temperature ( $T \cong 1,000 \text{ K}$ ) of the propellant gases when the projectile is "in bore" results in a subsonic Mach number behind the projectile. Therefore, at  $t = 0$  the propellant gases expand into the atmosphere, and, simultaneously, an expansion wave propagates into the muzzle, producing a sonic muzzle condition. The propellant gas flow regime is depicted schematically in Fig. 3. The predicted species mole

fractions for the propellant gas are given in Table I (provided by E. M. Schmidt, U.S. Army Ballistic Research Laboratory).

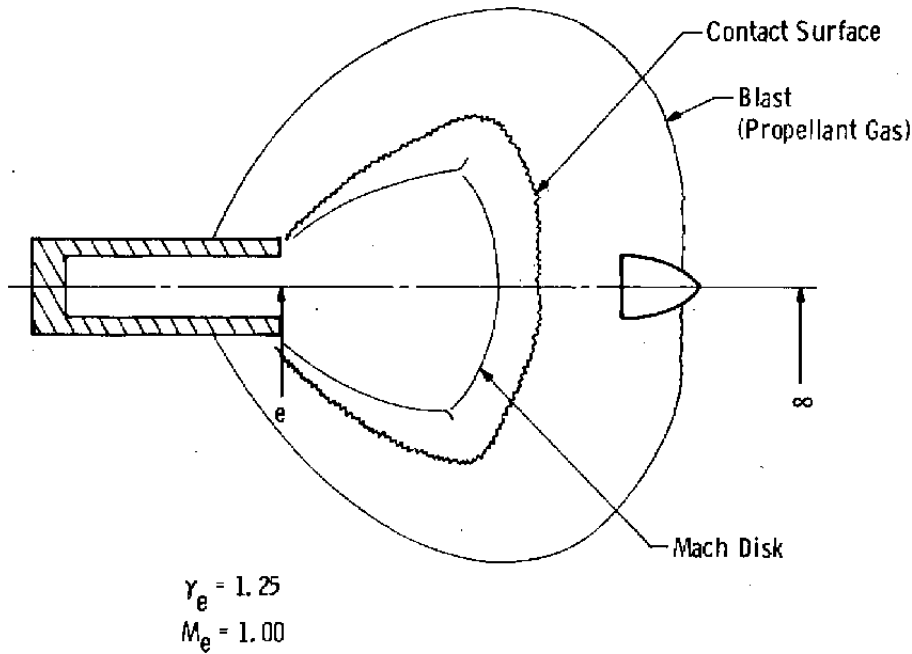


Figure 3. Propellant gas flow regime,  $t \geq 0$ .

Table 1. Predicted Species Mole Fractions for Propellant Gas

<u>Molecule</u>	<u>Mole Fraction</u>
CO	0.3964
H <sub>2</sub> O	0.1887
H <sub>2</sub>	0.1542
N <sub>2</sub>	0.1145
CO <sub>2</sub>	0.1443

For a launch velocity of 470 m/sec the measured exit pressure ratio was  $p_c/p_\infty = 70$  for the 20-mm cannon (Ref. 3). Variation of the propellant gas pressure with time at the muzzle was assumed to follow the form described in Ref. 2, and this variation is plotted in Fig. 4. For this calculation, as described in Ref. 2, the chemistry was assumed frozen at the mole fraction values listed in Table 1, and, appropriate to these values, a constant value of 1.25

was used for the ratio of specific heats. With isentropic flow conditions assumed, the variations of temperature and total number density with time at the muzzle exit are also plotted in Fig. 4.

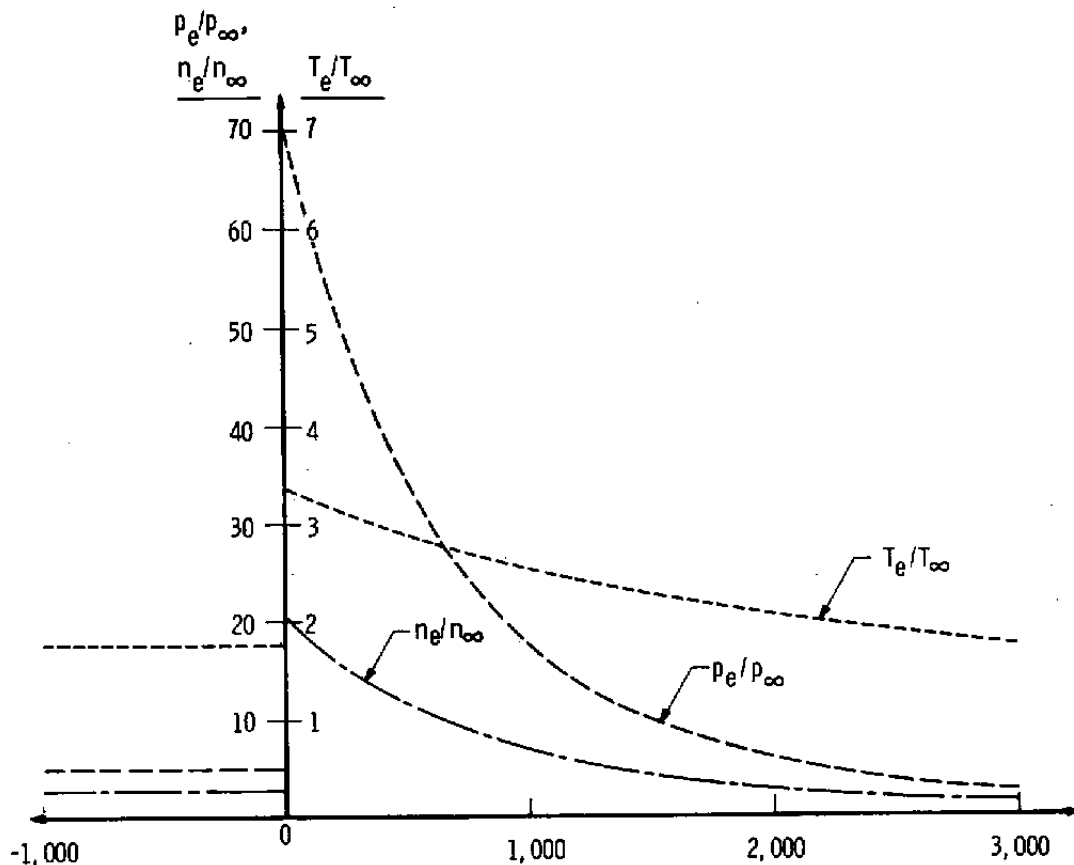


Figure 4. Estimate of exit plane flow properties.

## 2.0 EXPERIMENTAL SETUP AND OPERATION

### 2.1 CANNON AND DIAPHRAGM TEST ROOM ARRANGEMENT

The arrangement of the cannon, projectile catcher, laser system, and spectroscopic system within the diaphragm test room (DTR) is shown in Figs. 5, 6, and 7. The 20-mm Vulcan cannon is shown securely mounted to a lathe bed running the length of the room. The gun has a length of 152 cm, a chamber volume of 41.7 cm<sup>3</sup>, and a rifling twist of one turn in 25 calibers. Launch velocities of 470 m/sec were obtained by downloading the mass of WC870 propellant to 10 grams per round, and a standard, 98-gram training projectile was launched.

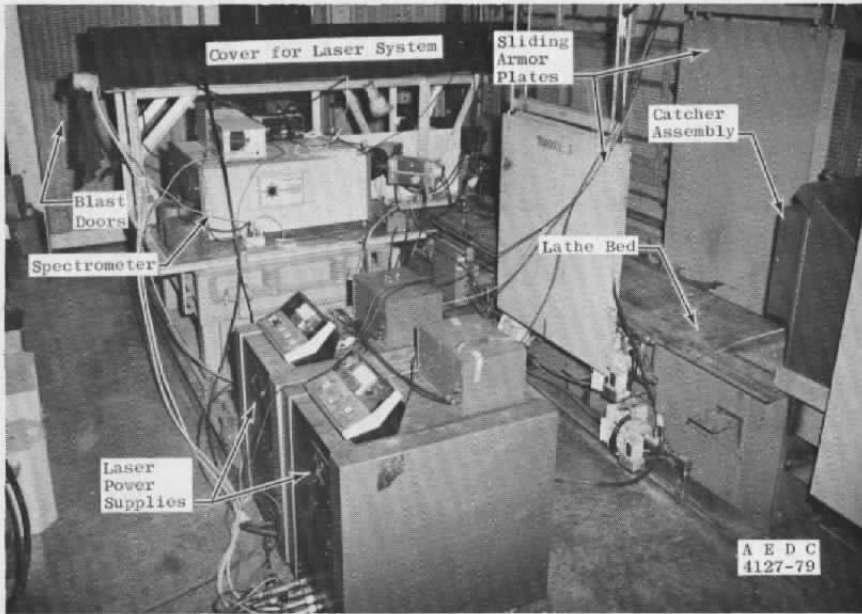


Figure 5. Experimental arrangement, view No. 1.

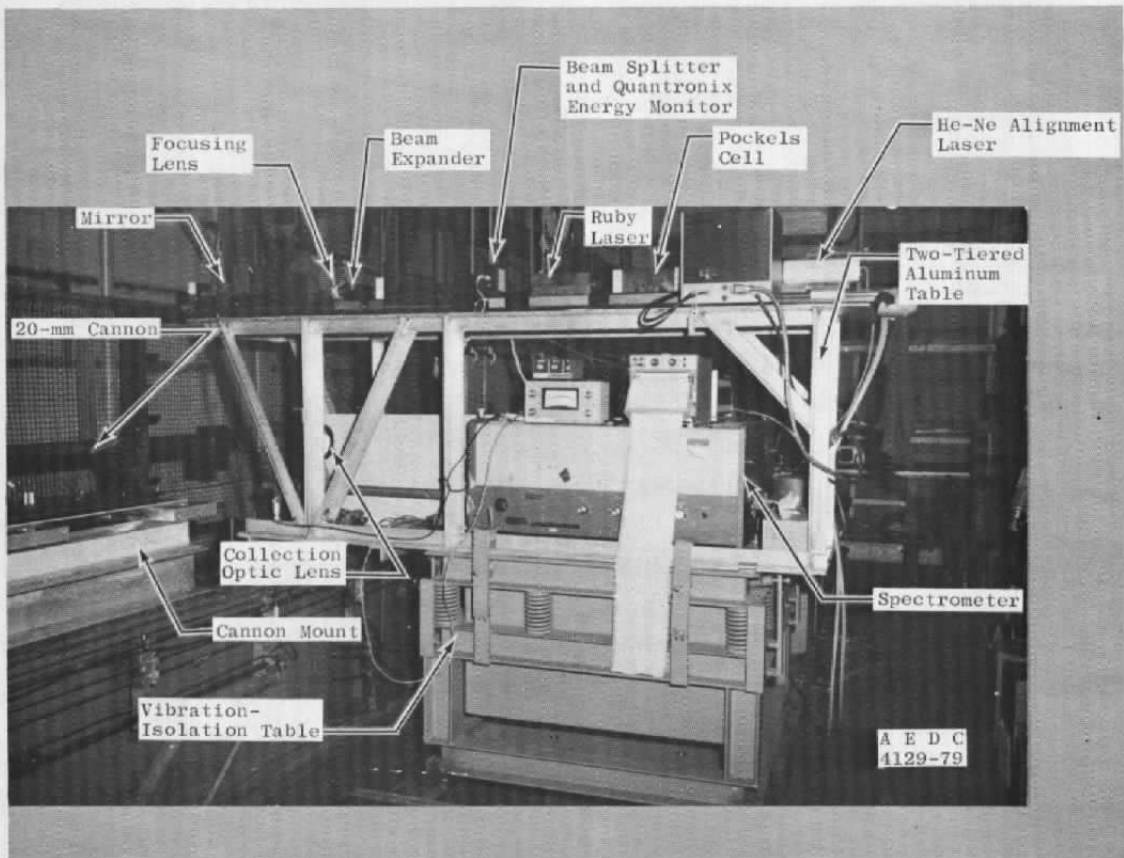


Figure 6. Experimental arrangement, view No. 2.

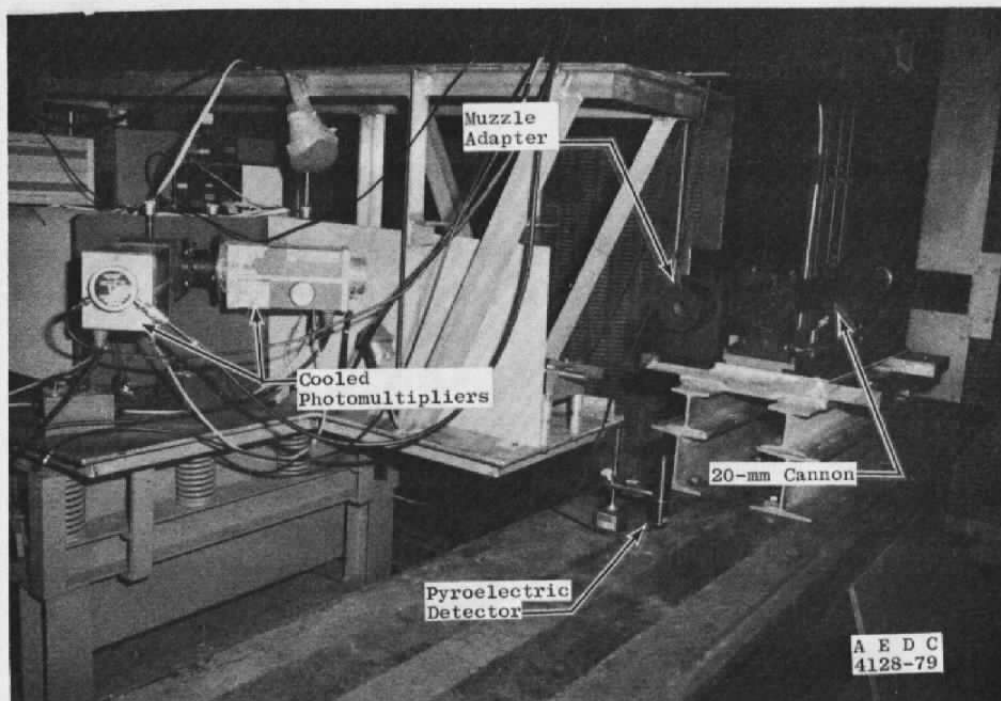


Figure 7. Experimental arrangement, view No. 3.

A muzzle adaptor having an overall length of 12 cm (see Fig. 7) was provided by the BRL to accommodate and shock mount an array of pressure transducers. Two Kistler 201 piezoelectric pressure transducers were spaced 62.5 mm apart, and the last transducer was 12.5 mm from the muzzle exit. The output of the transducers was recorded on Tektronix Type 7633 storage oscilloscopes. The time between pressure impulses recorded by the transducers was used to provide a measure of launch velocity, and the output of the transducer was also used to provide a trigger mechanism that initiated the laser firing and data acquisition sequence.

The front portion of the projectile catcher assembly can be seen in Fig. 5, and the assembly is shown schematically in Fig. 8. The catcher was designed by the BRL and fabricated at AEDC. The projectiles struck the 2-in.-thick armor plate, fragmented, and were deflected downward, to be easily stopped by the 15 to 20 cm of sand in the bottom of the catcher assembly.

In the interest of both personnel and equipment safety, sections of 1/2-in. (1.2-cm) armor plate suspended from rails were positioned along the sides of the projectile flight path and at the rear of the projectile catcher assembly. Furthermore, the three outer walls of the room were covered with steel blast mats. All data acquisition equipment and test personnel were

located outside the room, and the steel mesh blast doors of the room were always closed during cannon firings.

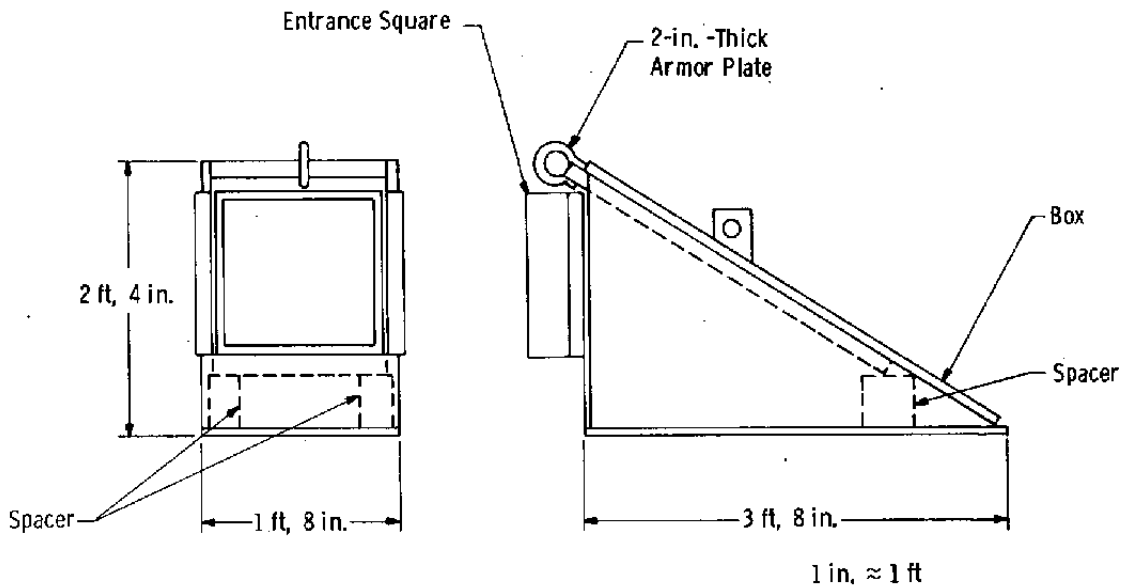


Figure 8. Projectile catcher assembly.

## 2.2 LASER SYSTEM

A Holobeam 600 series pulsed ruby laser was used for Raman excitation. The laser and associated optics were mounted directly above the spectrometer system as shown in Figs. 5 and 6. The 3/8-in. (0.95-cm)-diam laser beam was expanded in the ratio 3:1 and could be focused at various positions above the cannon axial centerline by adjustment of the 1,000-mm focal length laser focusing lens. A hard-coated, dielectric mirror deflected the laser beam through 90 deg, across the axial centerline of the cannon as near the muzzle exit plane as possible, into a pyroelectric energy receiver which provided a measure of laser beam transmission. The entrance to the pyroelectric energy detector was 15.5 in. (39.4 cm) below the cannon axial centerline. A thin quartz beam splitter mounted at the laser output diverted a few percent of the laser output energy to a Quantronix energy meter which measured variations in energy output. A beam splitter/filter/photomultiplier assembly was placed behind the rear mirror of the laser to monitor laser pulse shape as well as energy.

For Q-switched mode operation a Pockels cell was placed directly behind the laser head and was followed by a rear mirror assembly. In this configuration the laser system could deliver 3 Joules output at 6,943 Å with a pulse width of 20 nsec. For conventional mode operation the rear mirror assembly was placed directly at the rear of the laser head and the

Pockels cell was removed. In this configuration the laser system could deliver 25 Joules output at 6,943 Å with a pulse width of 600  $\mu$ sec.

### 2.3 SPECTROMETER SYSTEM

Raman scattered radiation was collected from an observation volume on the cannon axial centerline by a 4-in. (10.2-cm)-diam quartz lens which is shown in Fig. 5. The object distance was 17 in. (43.2 cm), and the image distance to the spectrometer entrance slit was 25.5 in. (64.8 cm), giving a magnification factor of 1.5.

A special housing was installed in front of the spectrometer entrance slit to hold a maximum of four filters and/or polaroid sheets. Schott RGN9 filters were used to block Rayleigh/Mie scattered radiation from entering the spectrometer. HN22 polaroid sheet was used to help block unpolarized particulate incandescence.

The spectrometer used for spectral dispersion was a 0.85-m Spex double spectrometer with 1,200 g/mm gratings blazed at 5,000 Å and a nominal reciprocal linear dispersion of 4.5 Å/mm. The normal, single exit slit assembly was replaced with a fixed-width (2-mm) double slit assembly. Two pairs of slits were available with 40-Å spectral separation at 7,020 Å and 20-Å spectral separation at 8,283 Å; these slits were used for rotational and vibrational Raman scattering, respectively. A spectrometer wavelength and transmission function calibration was performed for these slits.

Detection of the Raman scattered radiation transmitted by the double slits was achieved with a pair of cooled ( $-26^{\circ}\text{C}$ ) RCA-C31034A photomultipliers (see Fig. 7). Coupling to the slits was achieved with mirrors or a combination of mirrors and wedge prisms and lenses to image the slit radiation onto the photocathodes.

As shown in Figs. 5 and 6, the entire spectrometer system was mounted below the laser system on the same two-tiered aluminum table which was clamped to the top of a massive vibration-isolation table. This precaution was taken to prevent blast wave-induced vibrations from perturbing the optical system alignment.

### 2.4 DATA ACQUISITION SYSTEM

Various data acquisition methods were employed during these experiments. The basic technique was to integrate the photomultiplier tube (PMT) outputs during the interval of the PMT pulse. This method could be used for either Q-switch or conventional mode laser operation so long as the speed of the integration device was compatible with experiment.

The normal method for Q-switch mode operation was to integrate the 20-nsec-wide output pulses of the photomultipliers with a LeCroy Model 2250L fast integrator. The gate width for the integration was 100 nsec, centered about the photomultiplier pulse. A sequence of background radiation measurements was also made by the integrator following the laser firing. The outputs of the fast integrator and the pyroelectric detector were read by a microprocessor system which printed the results via a teletype following each cannon firing.

The normal method for conventional mode operation was to use the photon-counting technique. Photomultiplier signals were processed by Ortec Model 454 amplifiers, Model 436 discriminators, and a Model 774 counter. The data gate width was 60  $\mu$ sec. The photon counts and data gate duration were recorded by the microprocessor system for the laser firing and also immediately (160  $\mu$ sec) before the laser firing for a background measurement.

The microprocessor-based data system used in these experiments was configured to control both cannon firing and data acquisition. Because of the variety of data acquisition schemes required, the system was designed with a certain degree of flexibility to accommodate these variations. The three general control features required of the microprocessor system were: 1) "setup" and cannon firing; 2) data acquisition including intensity measurements, signal conversions, and retention of the detector outputs in the recording instruments; and 3) processor data input and printout, which involved the transfer of data from instruments to the processor and teletype (TTY) output of printed results. No computational processes other than conversion were required of the system.

Shown in Fig. 9 is a block diagram of those devices utilized in the system setup and cannon firing and synchronization. This phase was initiated with a start pulse from the processor in response to an input from the TTY keyboard. The charging of the laser capacitor was initiated by the start pulse, and the firing of the laser completed the initial phase of the complete cycle. Fig. 10 is a timing diagram for the first phase.

As shown in Figs. 9 and 10, a manual permissive was required prior to any subsequent automatic sequences. Charge detonation occurred upon contact closure on the control lines, but only if a permissive had been selected. Following the start signal from the processor the laser capacitor was charged to a preselected voltage. At this point a laser ready signal was generated in the control unit which in turn activated a relay closure for detonating the cannon charge. No further sequence progress occurred until the storage oscilloscope was triggered. Depending upon the time desired for data acquisition the trigger source was either the detonation pulse and the transducer precursor or the projectile clearance pressure pulse, and usually the signal from the transducer nearest the breech at the time of projectile passage was used. Display of both transducer signals on the oscilloscope with the sweep time



adjusted commensurate with the velocity and separation made possible the determination of the projectile speed as it left the muzzle. Usually the transducer temporal responses and separation were recorded on the storage oscilloscope and photographed, and these data served as a monitor of the cannon performance. Shown in Fig. 11 is one such typical photograph.

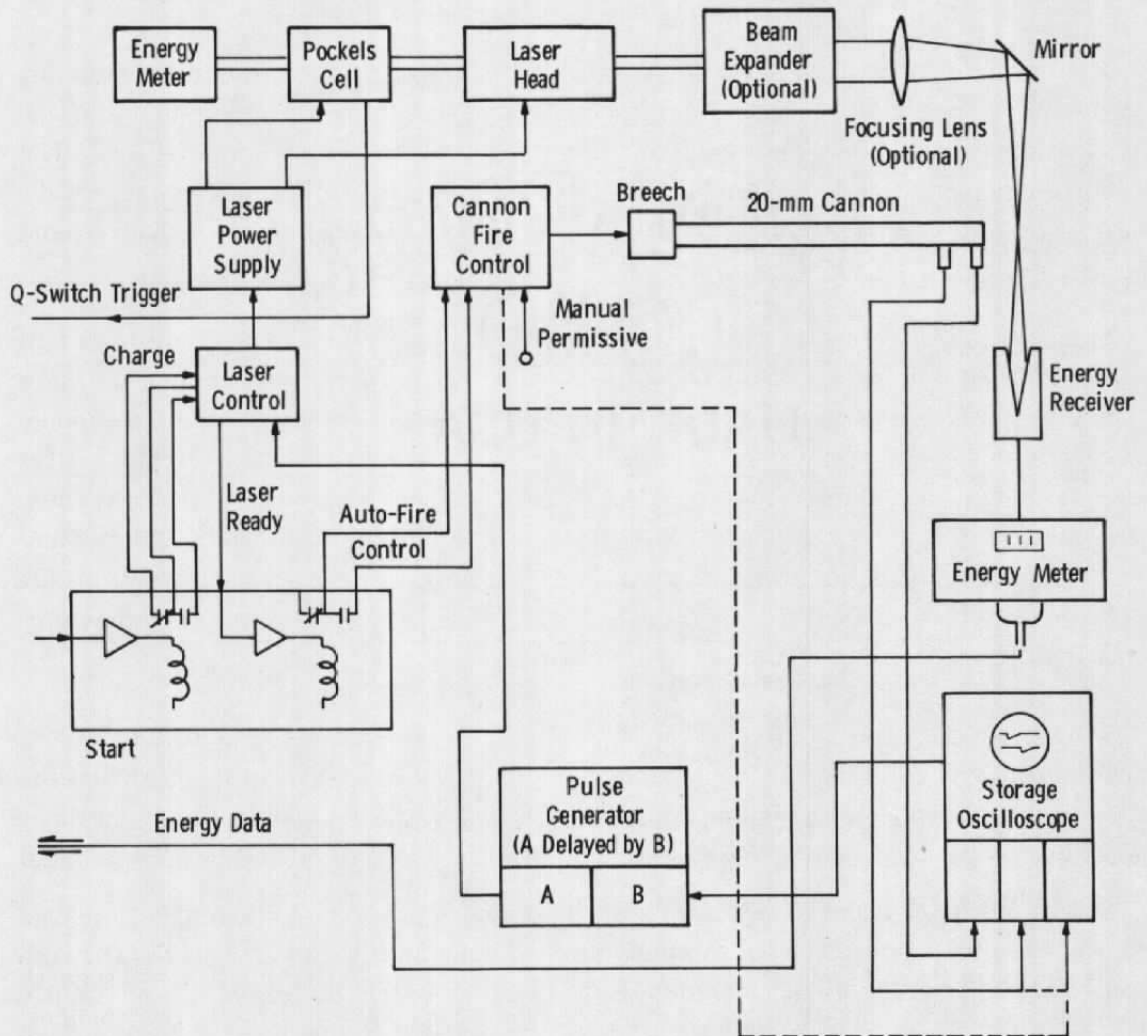


Figure 9. Block diagram of system setup for cannon firing and synchronization.

The leading edge of the oscilloscope gate was used to trigger a laser hold-off delay. The duration of this delay was chosen according to the desired instant of time for data acquisition concurrent with the laser energy pulse. The laser firing pulse initiates the flash lamp excitation, which precedes the actual energy pulse by 270 to 610  $\mu\text{sec}$ , depending upon laser mode. Actual data acquisition processes occur during the data interval sequence and

include background measurements. After data were acquired by the recording instruments, the processor input-output functions were completed, and the cycle was complete following implementation of a system reset.

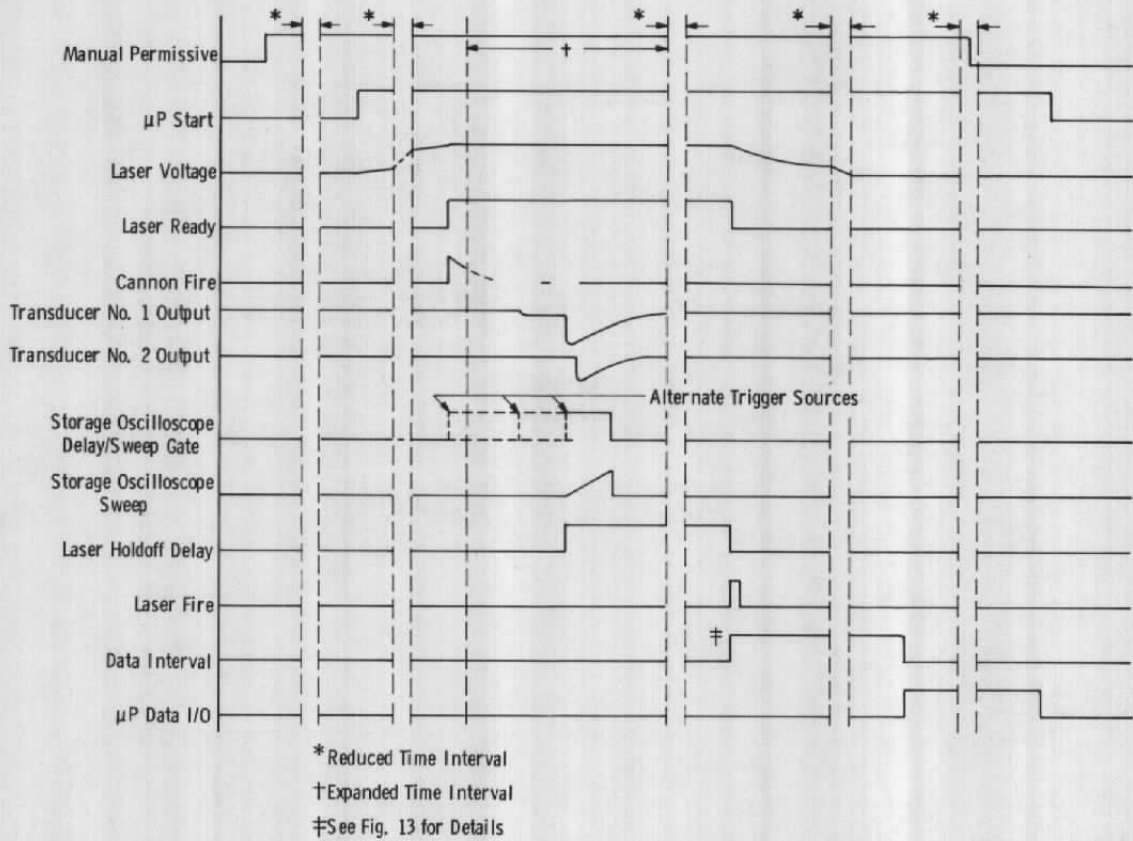
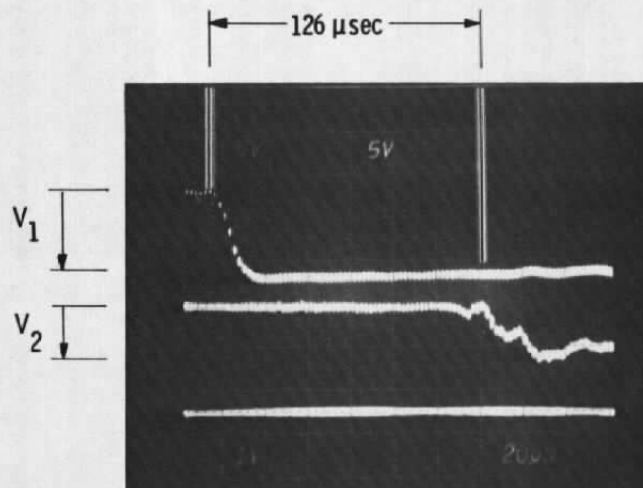


Figure 10. Timing diagram for major control events.

Shown in Fig. 12 is the block diagram of the system appropriate to the time of the data interval described above. The corresponding timing diagram is shown in Fig. 13. The data interval sequence began upon generation of the Q-switch trigger pulse, which occurred 610  $\mu\text{sec}$  after the flash lamp excitation. It should be noted that this delay corresponds to optimum laser performance and occurs approximately 250  $\mu\text{sec}$  before the energy pulse. A storage oscilloscope, which was used to monitor the timing features of the data acquisition functions, was triggered by the Q-switch pulse, and the oscilloscope gate pulse in turn triggered the gate pulse generator. System delays and an adjustable delay in the pulse generator accounted for the 250-nsec separation between the synchronization pulse and the Q-switch energy pulse and any additional delay differentials in the inter-connecting coaxial lines. The adjustable delays were selected to insure coincidence of the data gate and the

detector signals at the integrators. Differentials in lengths of cable and light paths between the laser energy monitor and the PMT signals were accounted for by adjustments in coaxial line length. These adjustments were made by applying appropriate signals to the storage oscilloscope and adjusting the delay on the gate generator while making repeated laser firings.



$$u_m = \frac{0.060 \text{ m}}{126 \mu\text{sec}} = 476 \text{ m/sec}$$

Figure 11. Typical transducer waveforms used for velocity measurements.

Referring again to Figs. 12 and 13, one can see that the oscilloscope gate was used to trigger a series of control pulses obtained from cascaded one-shot multivibrators. The data interval pulse (OS/1) was a flag used by the computer to indicate when data input to the integrator had been started and completed. Background data control (OS/2) was a gate to determine the number background trigger pulses generated. The background trigger pulses (OS/4) initiated the generation of additional data gates after the laser data had been obtained, and the converter cycle (OS/3) determined the rate at which background data were taken. The procedure was to follow the laser-scattering data with a series of background measurements of the same integration interval. After  $N \leq 31$  background pulses the sequence was terminated (OS/2), and the data interval (OS/1) flagged the processor to read the data from the memory of the integrator module, convert the results to decimal, and print the results.

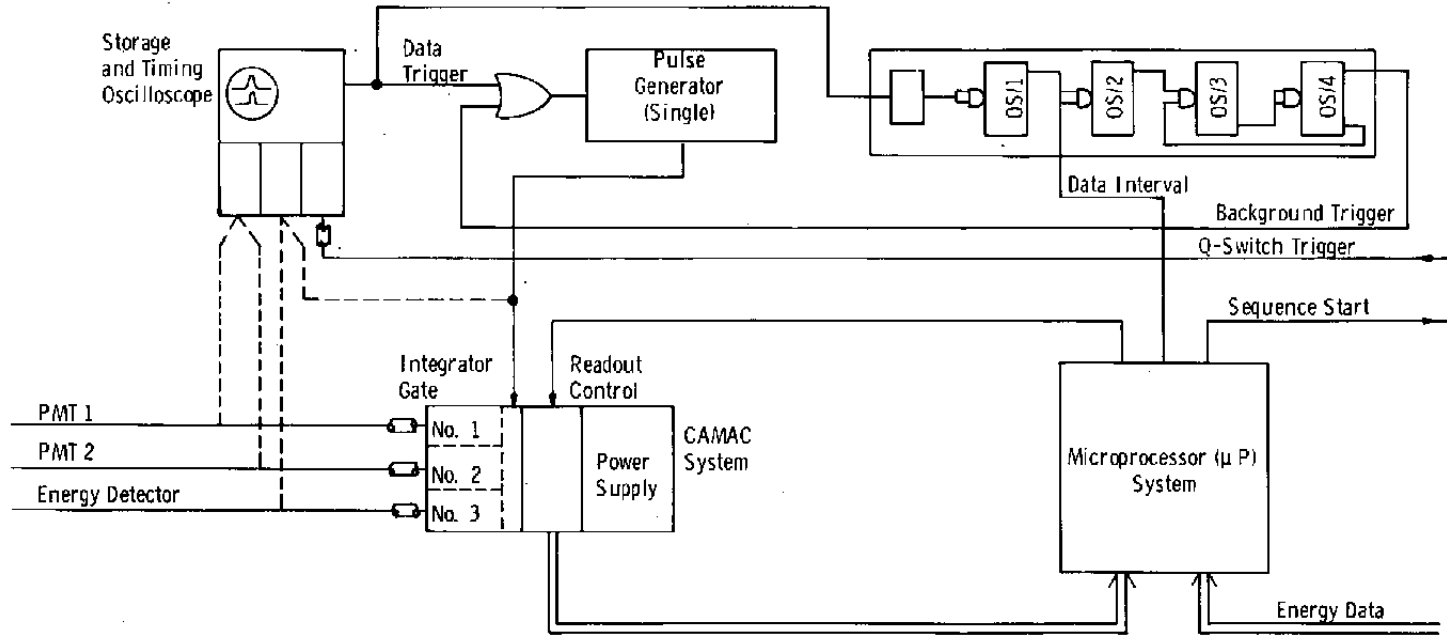


Figure 12. Block diagram of the electronic system applicable during the data acquisition interval; Q-switch mode/integrator.

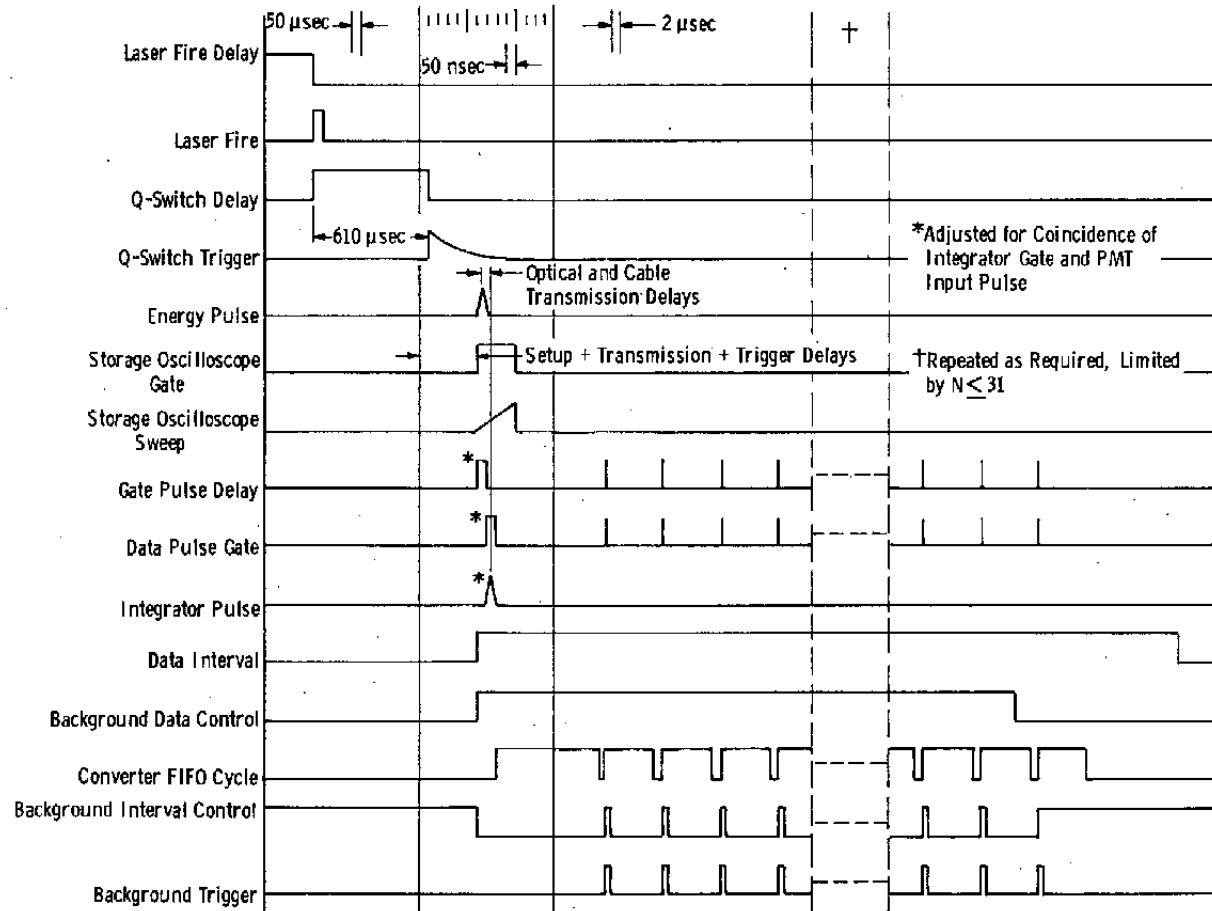


Figure 13. Timing diagram for data acquisition interval.

As noted elsewhere, particle incandescence limited the application of this technique, and an alternate method of using an unfocused beam and the conventional laser mode was implemented. The same basic system design was used with the following change. The gate to the integrator, as shown in Fig. 14, was obtained from what had been the gate trigger (OS/4). The width was selected such that the maximum gate output was less than approximately 1  $\mu$ sec. The Q-switch sync delay was reduced from 610 to 160  $\mu$ sec, and the interval between data pulses was adjusted (OS/3) to 12  $\mu$ sec. The effect was to obtain background data before the time of laser output and multiple data samples during the time of the laser output.

A third configuration (Fig. 15) was an adaptation of the previous arrangement except that a photon counter system was used instead of integrators. selectable background and data gates were used (OS/2 and OS/4, respectively) separated by a delay (OS/3) commensurate with time necessary to obtain peak energy from the laser. Separate background and data counters for both PM tubes were required in addition to two counters driven by a 10-MHz clock for measurement of the background and data intervals. Data reduction required weighting the background interval according to the duration of relative times of the two gate pulses. The interval gate (OS/1) again flagged the processor when the data were to be read into the computer and printed out.

In all cases the three configurations used the same technique during the startup cycle. The principal changes occurred during the interval cycle (OS/1) with the exception of different readout routines for the counters and integrators. The energy monitor required reading three BCD digits from the energy meter readout system.

### 3.0 LASER-RAMAN MEASUREMENT TECHNIQUE

#### 3.1 SPECTRA AND INTENSITY RELATIONS

When a gas is irradiated by an incident laser beam consisting of photons of energy  $h\nu_0$  ( $\nu_0 = c/\lambda_0$ ), a small portion of the light beam is scattered at frequencies other than  $\nu_0$ ; such an inelastic scattering phenomenon is known as Raman scattering (Refs. 11 through 14). The inelastic collisions between the laser beam photons and the gas molecules cause the molecules to undergo transitions to higher or lower energy levels with the result that light is scattered at lower or higher frequencies, respectively, than  $\nu_0$ . The lower frequency (longer wavelength) Raman scattering is commonly referred to as Stokes, and the higher frequency (lower wavelength) Raman scattering is called anti-Stokes.

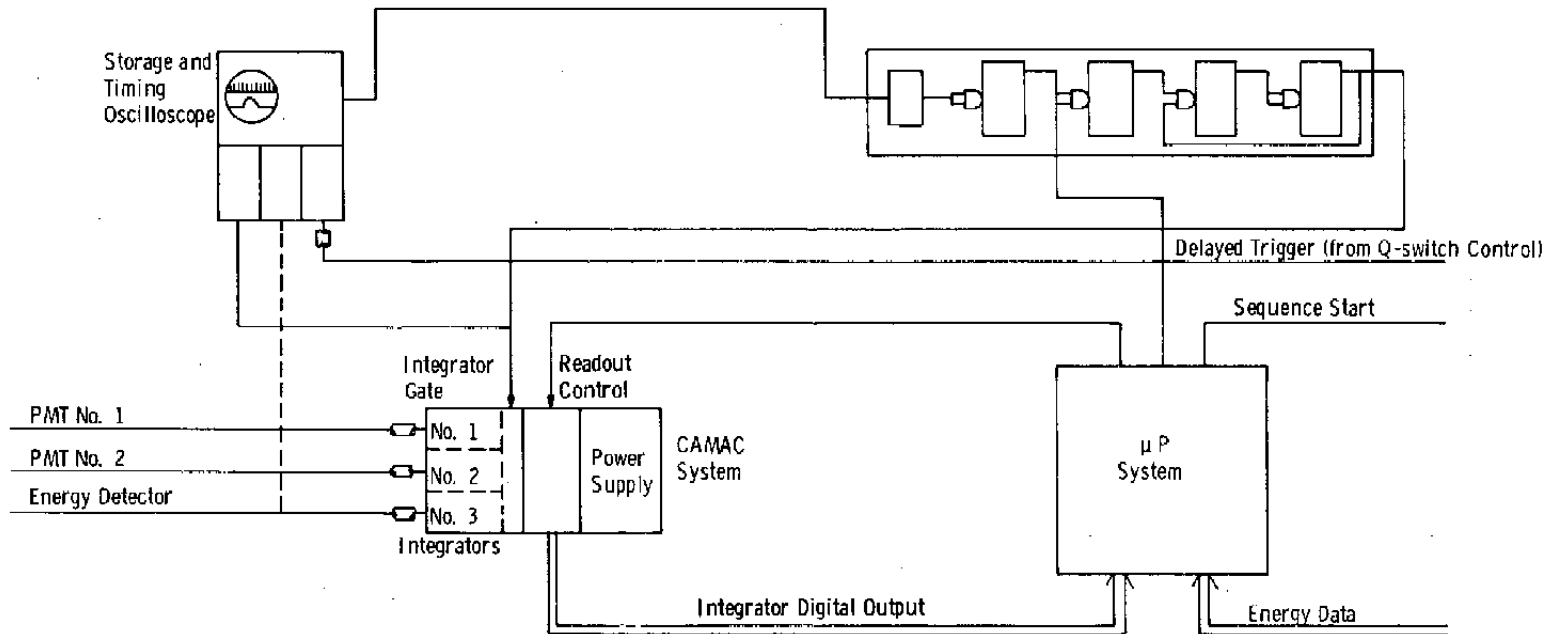


Figure 14. Block diagram of the electronic system applicable during the data acquisition interval; conventional mode/integrator.

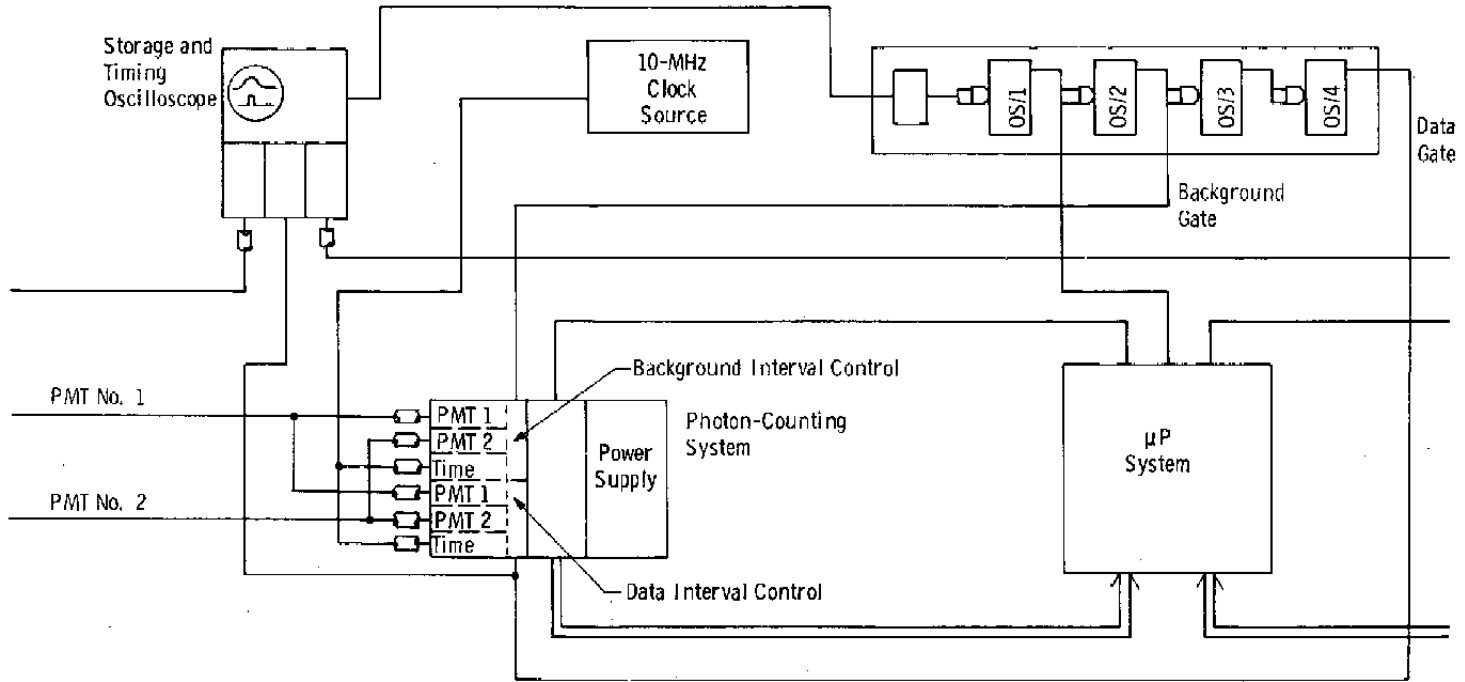


Figure 15. Block diagram of the electronic system applicable during the data acquisition interval; conventional mode/photon counting.



The nominal vibration-rotation Stokes band wavelengths for the major species of the muzzle blast flow field are given in Table 2 for a laser excitation wavelength of 6,943 Å. The H<sub>2</sub> and H<sub>2</sub>O wavelengths are beyond the sensitivity limits of the best available photomultipliers. The CO and N<sub>2</sub> bands are quite easily detected, closely located, and very similar in their dependence of spectral contour on temperature; also, the line-by-line calculation of the spectral bands is straightforward. Therefore, the CO and N<sub>2</sub> vibration-rotation bands were chosen for diagnostic purposes.

**Table 2. Nominal Wavelengths for Vibration-Rotation Stokes Bands of Propellant Gas Species for a Laser Excitation Wavelength of 6,943 Å.**

<u>Molecule</u>	<u>Wavelength, Å</u>
CO	8,159
H <sub>2</sub> O	9,302
H <sub>2</sub>	9,764
N <sub>2</sub>	8,284
CO <sub>2</sub>	7,684; 7,624

The intensity of each band is directly proportional to the species number density and is also a function of temperature. This can be expressed as

$$\begin{aligned}
 n(N_2) &= C_F(N_2) C_F(T, N_2) I_M(N_2, Q_0) \\
 n(CO) &= C_F(CO) C_F(T, CO) I_M(CO, Q_0)
 \end{aligned}
 \tag{1}$$

in which  $n$  is species number density,  $C_F$  is calibration factor, and  $I_m$  is measured intensity of the  $v = 0$  Q-branch.  $I_m$  is always a laser beam energy-normalized value.

The temperature-dependent correction factor,  $C_F(T, N_2)$ , is determined by using the Raman Spectral Program (RASP) to calculate for a range of temperatures the temperature-dependent intensities of the individual Raman lines of the bands and convolve the results with the spectrometer response function. Figures 14, 15, and 16 show the results of such a calculation for the relative N<sub>2</sub> and CO concentrations predicted for the propellant gas at temperatures of 300, 700, and 1,100 K. The temperature-dependent factor is calculated from

$$C_F (T, N_2) = I_c^o (N_2, Q_o) / I_c^t (N_2, Q_o)$$

$$C_F (T, CO) = I_c^o (CO, Q_o) / I_c^t (CO, Q_o) \quad (2)$$

in which superscripts o and t indicate calibration conditions and muzzle blast conditions, respectively. Subscript c indicates a calculated value of intensity.

The density-dependent factor,  $C_F (N_2)$ , is determined by calibration at room temperature, atmospheric pressure conditions.

$$C_F (N_2) = n^o (N_2) / I_m^o (N_2, Q_o) \quad (3)$$

The value for  $C_F(CO)$  is determined through knowledge of the relative scattering cross sections.

$$R_\sigma = \sigma (N_2, Q) / \sigma (CO, Q) \quad (4)$$

and the relative spectral sensitivity of the optical system at the nominal wavelengths of the bands.

$$R_s = \frac{I_s^o (8,283 \text{ \AA})}{I_s^o (8,155 \text{ \AA})} \quad (5)$$

Therefore,

$$C_F (CO) = C_F (N_2) R_\sigma R_s \quad (6)$$

Close observation of the calculated spectral profiles shown in Figs. 16 through 18 reveals that the relative intensities of the  $N_2$  Stokes band  $v = 0$  and  $v = 1$  Q-branches are functions of temperature. Using RASP, one can calculate the ratio of the intensities,

$$R_v = I_c (N_2, Q_1) / I_c (N_2, Q_o) \quad (7)$$

and the result of such a calculation is given in Fig. 19. Therefore, using the double slit spectrometer setup to simultaneously measure the intensities of the  $v = 0$  and  $v = 1$  Q-branches, one can determine a temperature using the curve of Fig. 19.

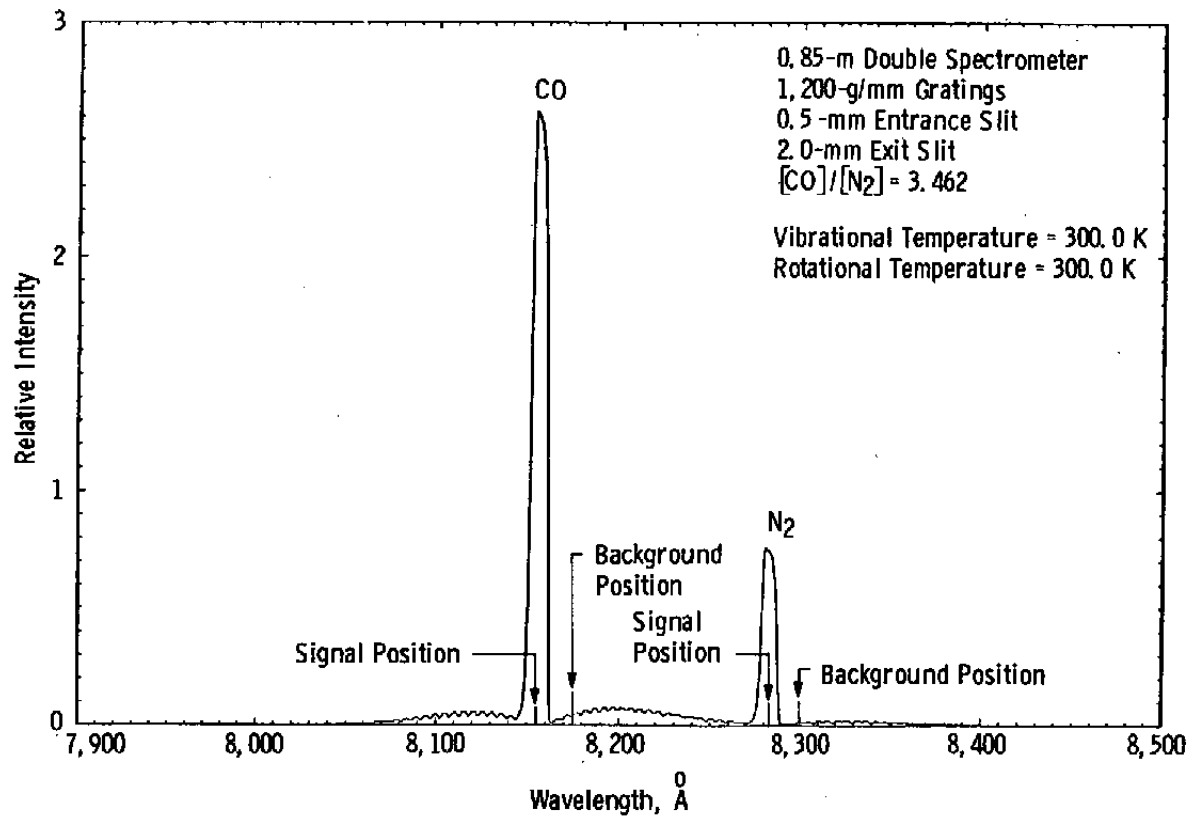


Figure 16. N<sub>2</sub> and CO vibration-rotation bands at T = 300 K.

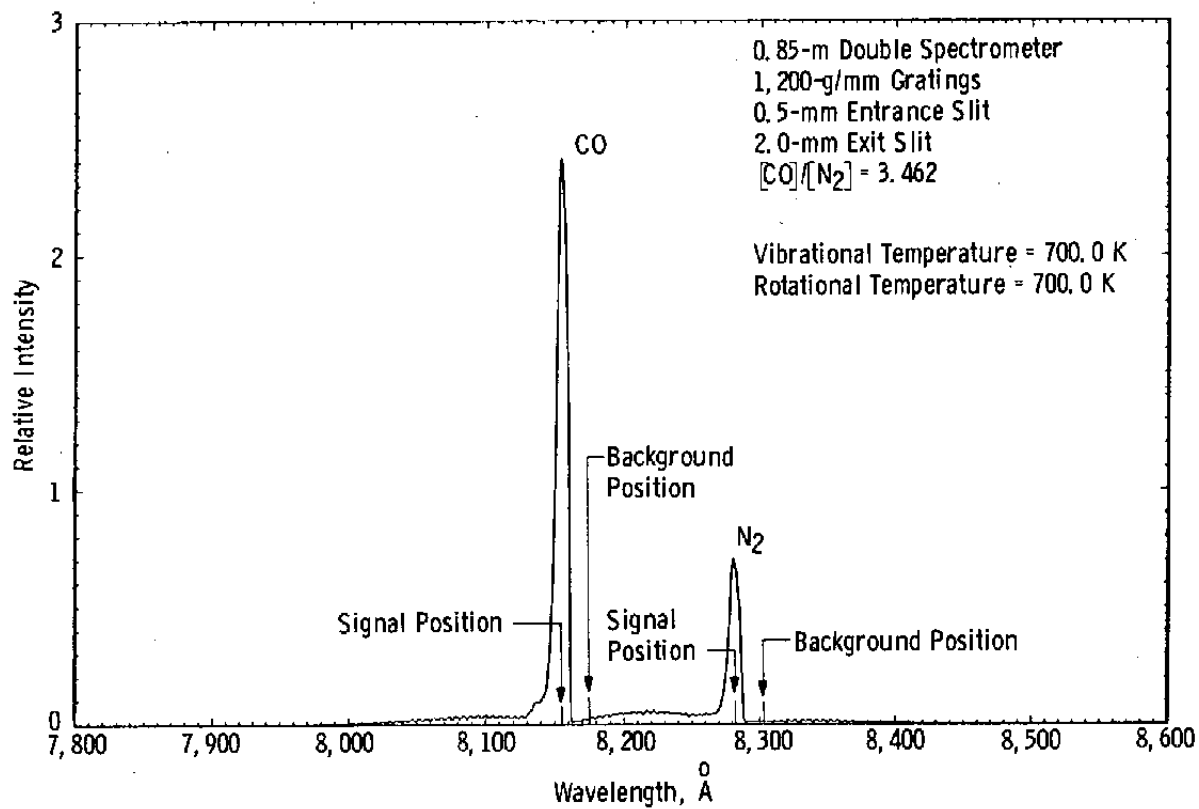


Figure 17. N<sub>2</sub> and CO vibration-rotation bands at T = 700 K.

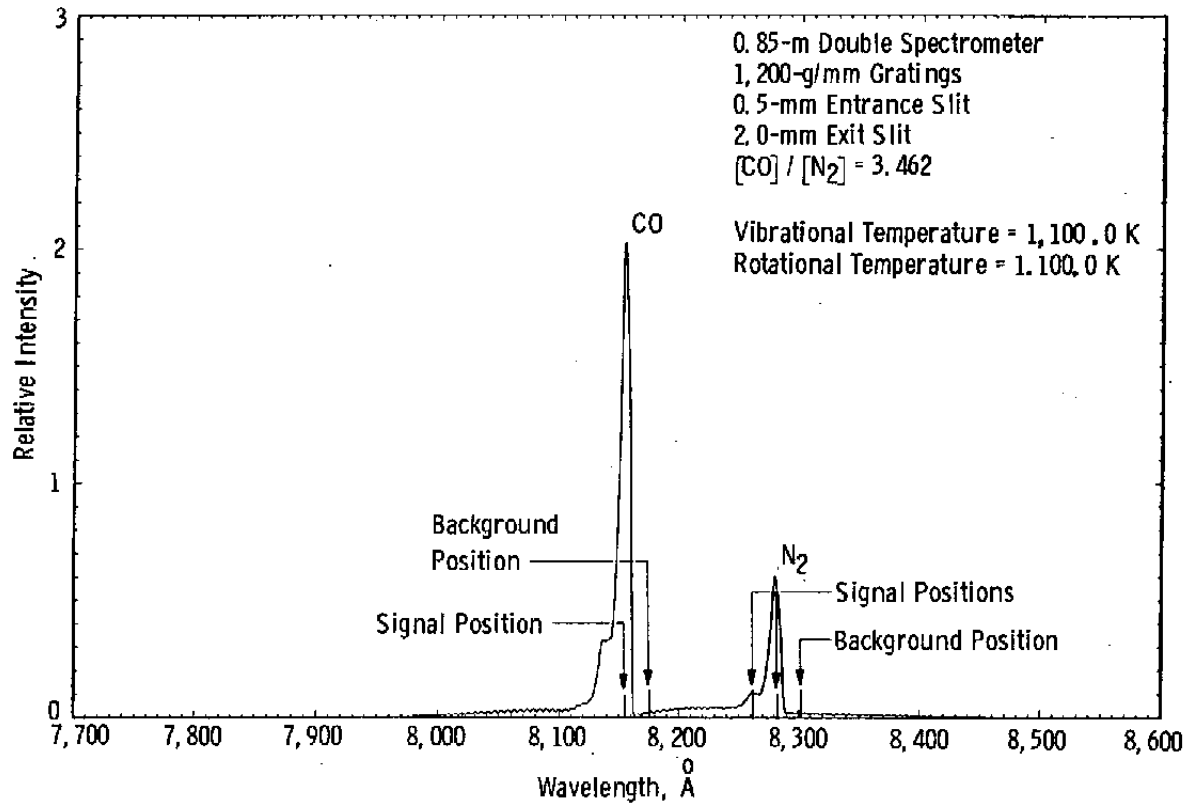


Figure 18. N<sub>2</sub> and CO vibration-rotation bands at T = 1,100 K.

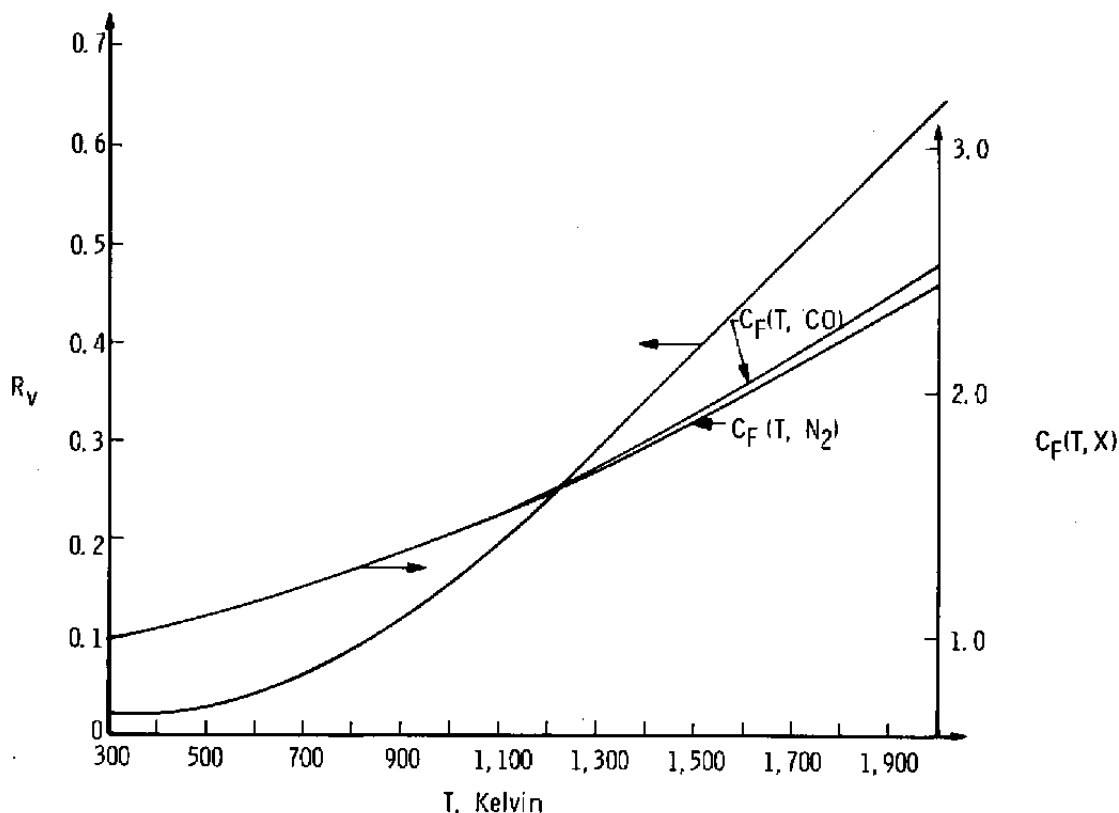


Figure 19. Calculated intensity ratio,  $R_v$ , and temperature-dependent correction factors,  $C_F(T, X)$ , as function of temperature.

An alternate method of temperature measurement is to use the pure rotational Raman structure rather than the vibration-rotation bands. The details of this method are discussed in detail in Refs. 15 and 16. Briefly, the pure rotational Raman structure is a result of photon-molecule collisions that cause only rotational level transitions rather than vibrational level changes. A RASP calculation of the Stokes rotational Raman spectra of  $N_2$ ,  $CO$ , and  $CO_2$  at 300, 700, and 1,100 K is shown in Figs. 20, 21, and 22, respectively. The species mole fractions were those predicted in Table 1 for the propellant gas flow regime of the muzzle blast. The change of the band profile with temperature is readily observed.

The  $H_2O$  rotational structure is too weak and widespread (Ref. 16) to require consideration. Although  $H_2$  has an intense rotational structure, its lines are widely spaced, and the first Stokes line lies at  $7,117 \text{ \AA}$ , which is beyond the spectral region presently being considered.

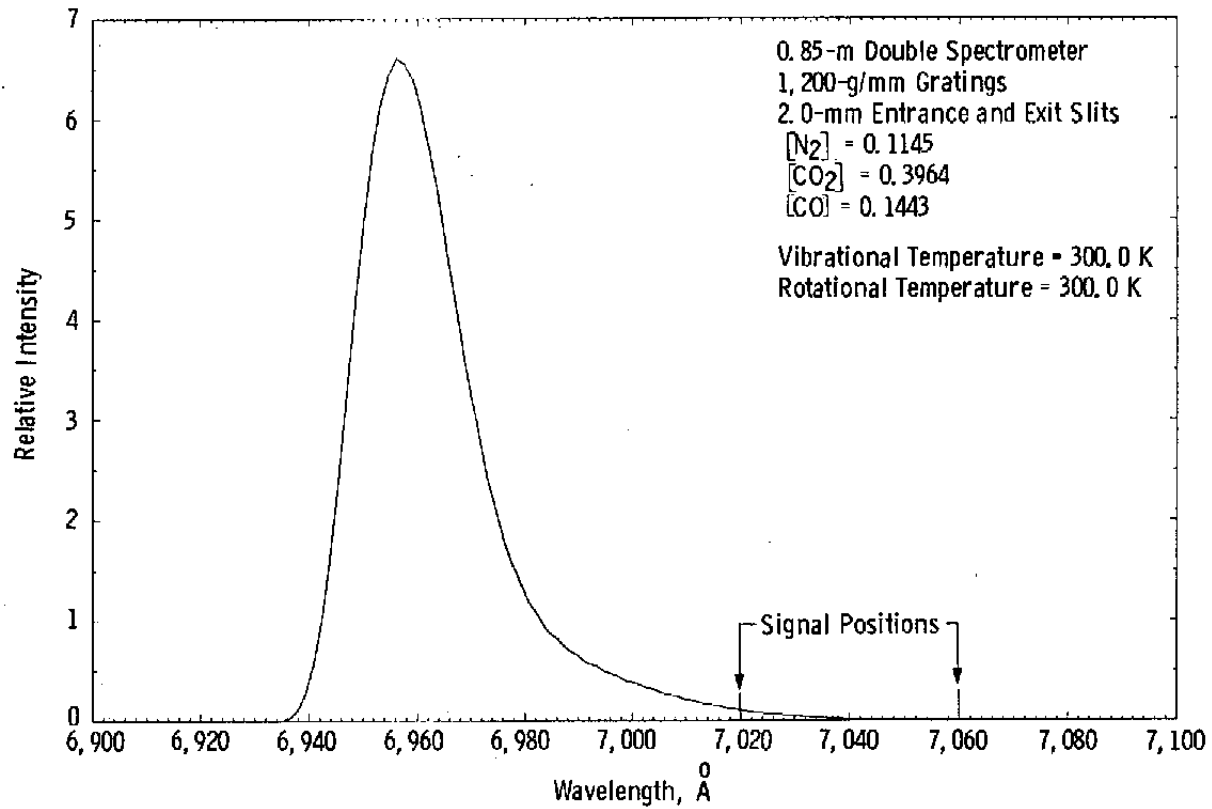


Figure 20. N<sub>2</sub>, CO, and CO<sub>2</sub> rotational Raman structure, T = 300 K.

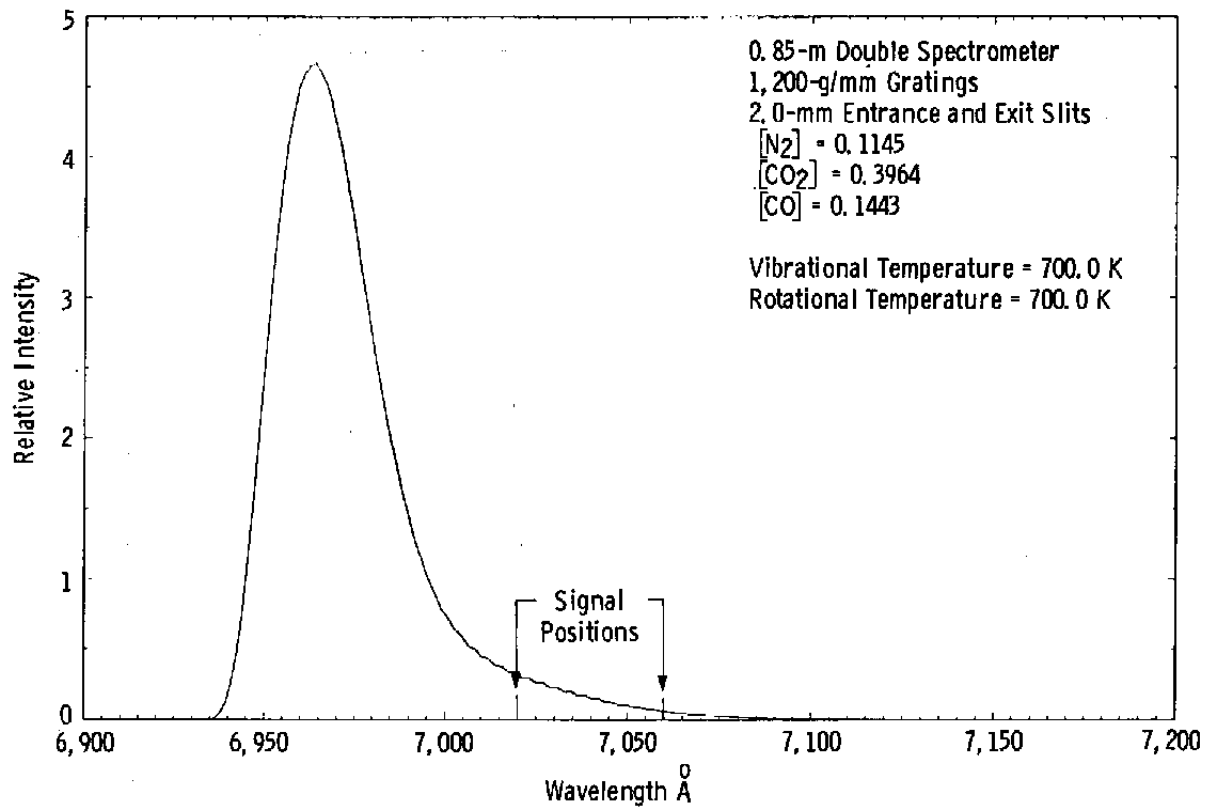


Figure 21. N<sub>2</sub>, CO, and CO<sub>2</sub> rotational Raman structure, T = 700 K.



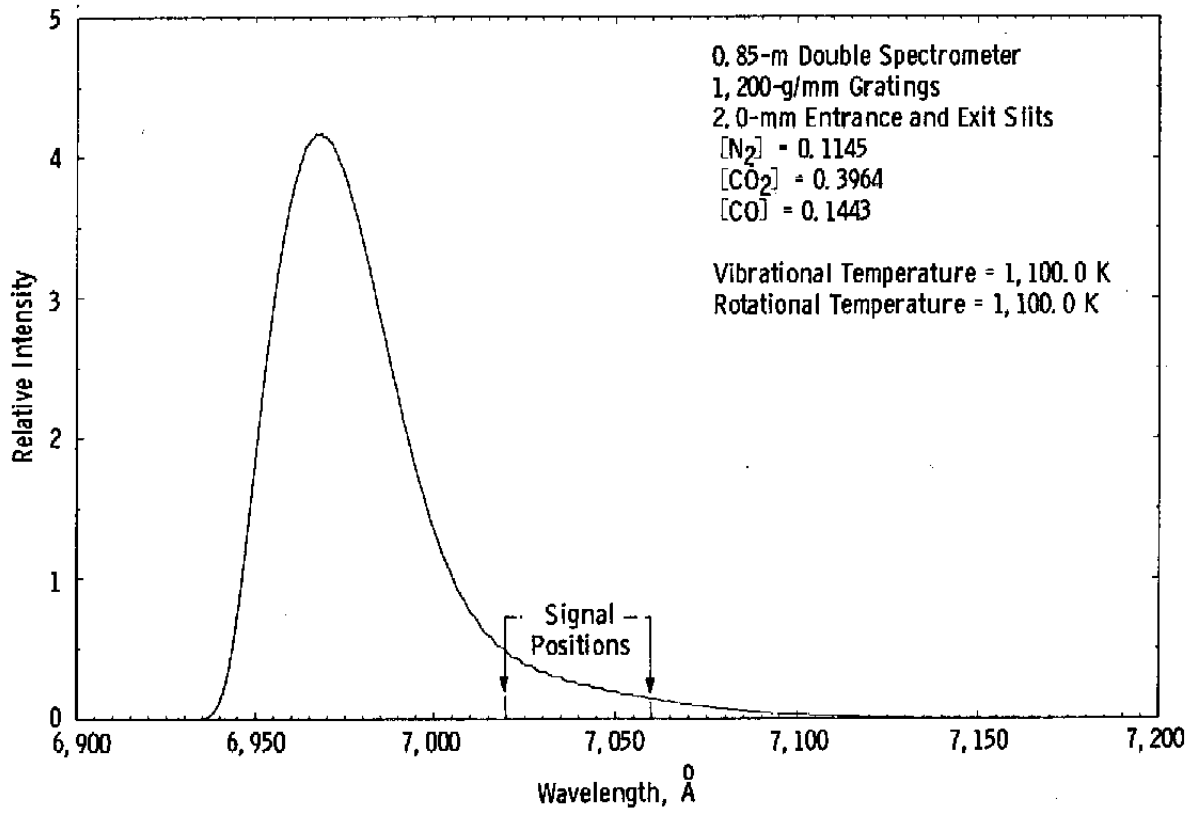


Figure 22. N<sub>2</sub>, CO, and CO<sub>2</sub> rotational Raman structure, T = 1,100 K.

Using a double slit arrangement allows sampling two portions of the spectral band simultaneously, and the ratio of intensities is primarily a function of temperature. There is also a dependence on species mole fractions; however, for the species mole fractions and temperature range anticipated for the muzzle blast flow this dependence is small, as can be seen in Fig. 23. The intensity ratios plotted as a function of temperature in Fig. 23 were calculated using RASP. These curves and measured values of intensity ratio permit determination of temperature.

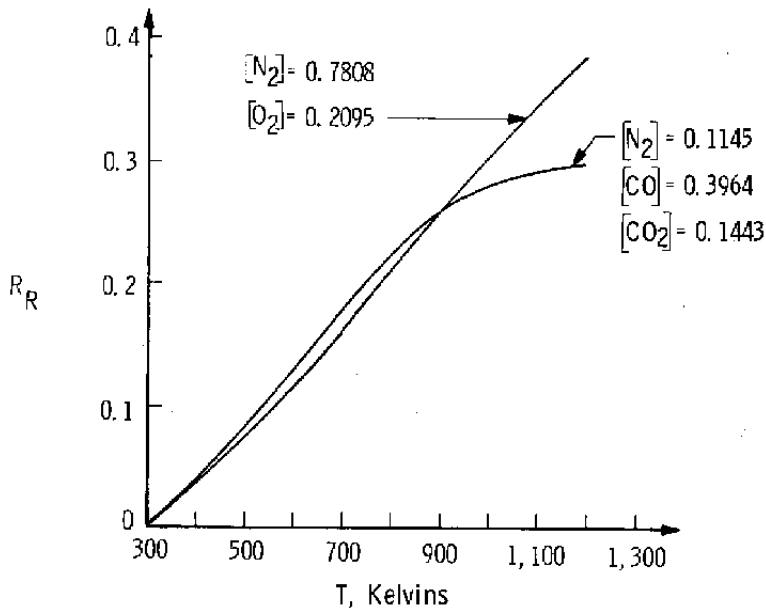


Figure 23. Calculated intensity ratio,  $R_R$ , as a function of temperature.

### 3.2 CALIBRATIONS

Prior to each test period a series of calibrations of the laser-Raman system was completed. The energy output of the laser was varied over a wide range, and all energy detector readings were recorded. This provided a calibration of the laser as well as determining an average transmission of the laser beam through the atmosphere to the pyroelectric detector. Values of  $C_F(N_2)$  were also measured for each photomultiplier, and this measurement also provided a direct measure of the relative sensitivities of the tubes at 8,283 Å. A similar procedure provided the relative sensitivity at 7,000 Å for rotational Raman measurements. Atmospheric number density was determined from atmospheric pressure and room temperature values. Relative humidity values permitted calculation of a dry air number density, and the  $N_2$  mole fraction was assumed to be 0.7808.

Following experiments with the double slit spectrometer system, the cannon was temporarily removed, and a tungsten strip standard lamp was placed such that the ribbon filament was at the observation volume of the collection optics system. The relative spectral response of each tube over the 3,500- to 8,300-Å range was obtained as well as the absolute response of each tube to a known spectral radiance. The linearity of the tubes was also verified using neutral density filters.

### 3.3 DATA REDUCTION

For the measurement of N<sub>2</sub> and CO densities the spectrometer wavelength dial was set such that the  $\nu = 0$  Q-branch intensity was monitored with one detector and a background radiation intensity was monitored with the other detector. The background was monitored at 19.6 Å beyond the spectral location of the  $\nu = 0$  Q-branch, and the background positions are noted on the spectral profiles of Figs. 16 through 18. Energy-normalized, background-corrected intensities were then used in Eqs. (1) to determine number densities. The temperature-dependent correction factors,  $C_F(T, N_2)$  and  $C_F(T, CO)$ , were obtained from Fig. 19 using either a predicted or measured temperature.

For a temperature measurement using the N<sub>2</sub> vibration-rotation band, the spectrometer wavelength dial was adjusted such that the  $\nu = 0$  Q-branch intensity was monitored with one detector while the  $\nu = 1$  Q-branch intensity was monitored with the other. These spectral locations are also noted in Figs. 16 through 18. If background radiation was repeatable from cannon firing to cannon firing, then the background level determined during N<sub>2</sub> density measurement could be used for background correction of both the  $\nu = 0$  and  $\nu = 1$  Q-branch intensities. This, of course, assumes a continuum background over the wavelength interval of interest. The ratio of the background-corrected intensities,

$$R_\nu = \left[ I_m^t(N_2, Q_1) / I_m^t(N_2, Q_0) \right] C_{F\nu} \quad (8)$$

could then be used with Fig. 19 to determine a temperature.

For a temperature measurement using the rotational Raman structure, the double slit separation was changed, and the spectrometer wavelength dial was adjusted such that Raman radiation at 7,020 and 7,060 Å was monitored by the detectors. These wavelength locations are shown on the spectral profiles in Figs. 20 through 22. Corrections for laser-induced background radiation cannot be conveniently made for the rotational structure. The ratio of the measured intensities,

$$R_R = \left[ I_m^t(7,060 \text{ Å}) / I_m^t(7,020 \text{ Å}) \right] C_{FR} \quad (9)$$

can be used with the plots of Fig. 23 to determine temperature.

## 4.0 DISCUSSION

### 4.1 CHRONOLOGY OF EXPERIMENTS

Initial Raman measurement attempts utilized the Q-switch mode of laser operation with the beam tightly focused on the muzzle axial centerline. Throughout the propellant flow regime the laser beam transmission was only a few percent, and the photomultiplier tubes were saturated even at minimum high voltage settings. The transmission of a continuous HeNe laser beam through the flow field at the muzzle exit plane revealed a nominal 60- to 80-percent transmission during the 0- to 3,000- $\mu$ sec interval after the projectile left the muzzle. The ruby laser beam expander was removed to increase the size of the beam focal volume and thereby decrease power density at the focal volume. Beam transmissions then increased to the 60- to 80-percent range observed with the HeNe laser. It was concluded that the particulate concentration in the flow field was sufficiently high to lower the gas breakdown threshold below the power densities being used with the focused, Q-switched beam.

Subsequent measurements utilized the Q-switch mode, but the laser focusing lens was shifted backwards along the optical rail to provide a beam diameter of 0.5 in. (1.2 cm) at the muzzle axial centerline. Beam transmissions of 60 to 90 percent were obtained in the 1,000- to 6,000- $\mu$ sec region of the flow (see Fig. 24). However, photomultiplier signals remained nearly two orders of magnitude higher than expected for the predicted gas densities of the flow field. It was suspected that laser-induced particulate incandescence (Ref. 17) was responsible for the high signal levels.

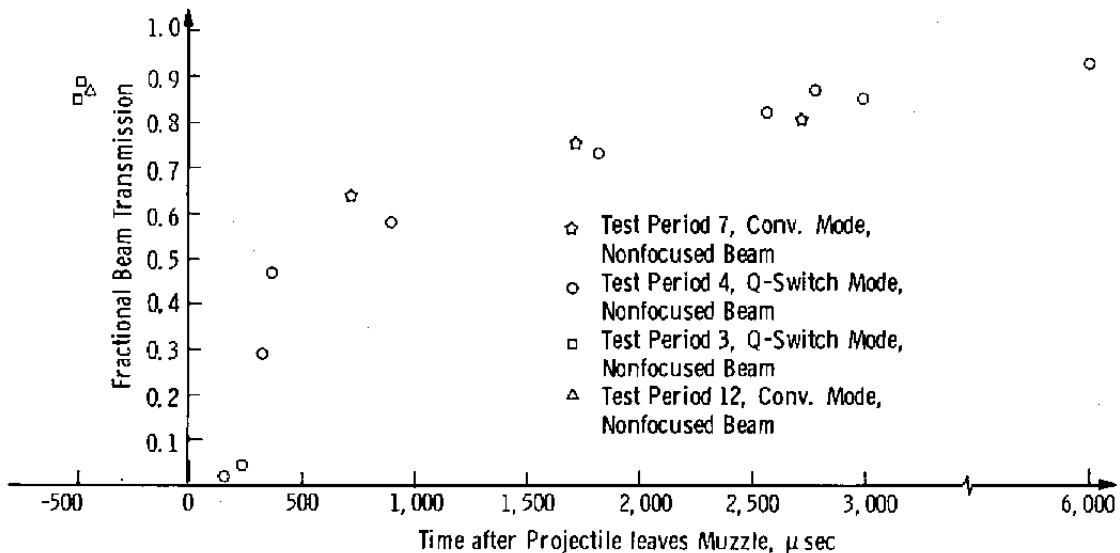


Figure 24. Fractional laser beam transmission as a function of time.

A possible solution to the laser-induced particulate incandescence problem as suggested in Ref. 17 was to increase laser power density. However, in the present case of high particulate levels the gas breakdown phenomena prevented this possibility. Utilizing the polarization properties of the vibration-rotation Raman signals produced only about a factor of two improvement in the signal-to-noise ratio. Therefore, the alternate approach of drastically lowering the laser beam power density by using the conventional mode of laser operation was selected. This was deemed reasonable because cannon firings without laser operation produced no detectable signals from muzzle blast self-radiation.

Experiments with the conventional mode beam focused at the muzzle exit plane revealed high laser transmission (75 to 85 percent), but laser-induced particulate incandescence levels remained high. As shown in Fig. 25 at the focused beam power density of  $\approx 10^7$  watts/cm<sup>2</sup>, the laser-induced particulate incandescence was more than two orders greater than the Raman N<sub>2</sub> calibration signal level at atmospheric conditions. Changing the position of the laser focusing lens to increase the laser beam diameter and thereby decrease power density to  $\approx 10^5$  watts/cm<sup>2</sup> reduced the incandescence linearly. However, the Raman N<sub>2</sub> calibration signal level was reduced only a factor of five because of the geometry of the collection optics. Of course, spatial resolution was sacrificed.

An optimum arrangement was reached by 1) removing the laser beam focusing lens and using the unfocused beam at 12 Joules per pulse, 2) using a Polaroid filter in the collection optics oriented to pass only light polarized parallel to the polarization of the laser beam, and 3) using a 2-mm entrance slit height and a 500- $\mu$ m width. In order to miss the edge of the muzzle adaptor the center of the beam was positioned 0.512 in. (1.30 cm) from the muzzle exit plane. The spatial volume observed by the spectrometer was a 1.33-mm-high, 0.33-mm-wide, 5.7-mm-long box centered on the axial centerline of the cannon.

Because of the existence of the laser-induced particulate incandescence it was impossible to obtain reliable temperature measurements utilizing the rotational structure. An attempt was made to use the N<sub>2</sub> vibration-rotation band for a temperature measurement by making an on-band measurement with the double slit system set to detect the  $v = 1$  and  $v = 0$  Q-branch intensities and by making a subsequent measurement of the  $v = 0$  Q-branch and the off-band incandescence intensity. However, the shot-to-shot variations of the laser-induced particulate incandescence level were too large to obtain reliable measurements.

Attempts to make temperature measurements were therefore abandoned, and the experiments were directed toward obtaining N<sub>2</sub> and CO number densities. Measurements were made with the double slit assembly set to simultaneously monitor the  $v = 0$  Q-branch and off-band radiation. At least five cannon firings were made and the results averaged to obtain a data point. The results of these measurements are shown in Fig. 26.

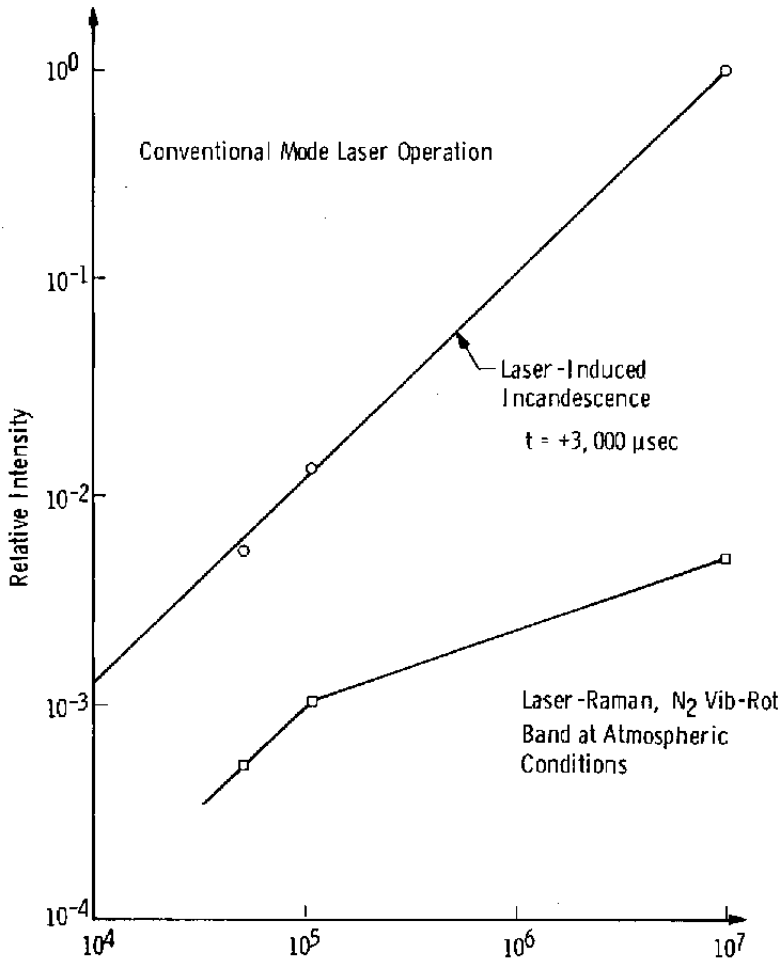


Figure 25. Laser power density at focal volume, watts/cm<sup>2</sup>.

Measurements were later made in the anti-Stokes Raman region at a wavelength ( $\lambda$ ) equal to 5,976.5 Å, which is the  $v = 0$ ,  $N_2$  Q-branch position. These measurements were made in an attempt to circumvent the incandescence problem by moving to the lower wavelength portion of the spectrum. Indeed, the laser-induced particulate incandescence level was reduced by a factor of 36.9 (corrected for optical system spectral sensitivity differences). However, the gas temperature in the muzzle blast region was not sufficiently high to provide a detectable anti-Stokes signal.

An attempt was also made to utilize an image intensifier/vidicon/triple slit system to simultaneously measure two on-band signals and one off-band signal. However, the sensitivity of the system was not sufficient because of the poor spectral response in the red, and of course it was not possible to offset the spectral sensitivity loss by increasing laser power density.

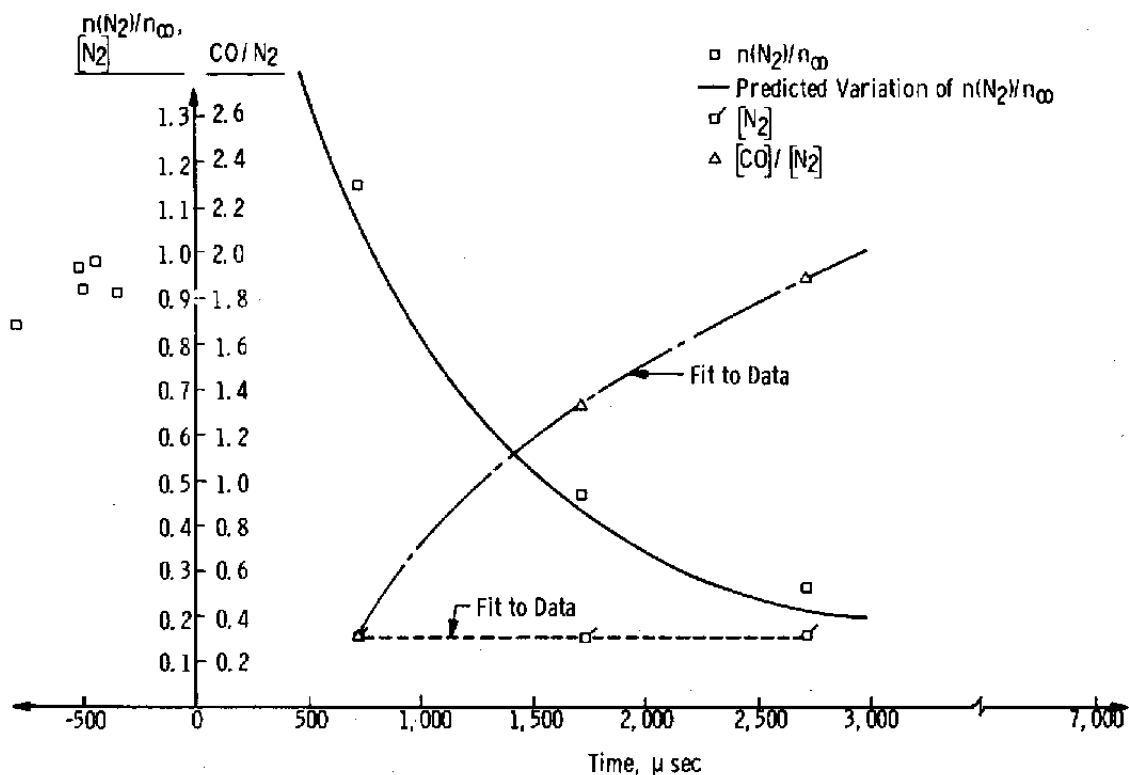


Figure 26. Measured relative number densities as a function of time.

## 4.2 RAMAN RESULTS AND COMPARISONS WITH PREDICTIONS

The laser beam transmission measurements shown in Fig. 24 indicate that any Raman measurements attempted within 600  $\mu\text{sec}$  of projectile clearance of the muzzle would probably be susceptible to multiple scattering effects (Ref. 18). Therefore, measurements were made in the  $t + 600 \mu\text{sec}$  propellant gas flow regime and in the precursor flow. In order to reduce the propellant gas flow data the temperature values predicted using the isentropic flow assumption and an assumed  $T_e = 1,000 \text{ K}$  had to be used, and these values are plotted in Fig. 4. As shown in Fig. 26, the variation of the ratio of  $N_2$  density to the ambient density  $[n(N_2)/n_\infty]$  follows the predicted variation very closely. The predicted variation of the ratio of total number density to the ambient density ( $n_e/n_\infty$ ) permits a mole fraction of  $N_2$ ,  $[N_2]$ , variation to be calculated, and it is also plotted in Fig. 26. It can be seen that a near constant mole fraction of  $N_2$  (0.15) exists from 700 to 2,700  $\mu\text{sec}$ . The measured values of the CO-to- $N_2$  mole fractions,  $[CO]/[N_2]$ , are also shown in Fig. 26, and the mole fraction of CO increases from 0.045 at 700  $\mu\text{sec}$  to 0.29 at 2,700  $\mu\text{sec}$ .

Precursor flow measurements of the ratio of  $N_2$  density to ambient density are also shown in Fig. 26. At  $-450 \mu\text{sec}$  the values are clustered at  $\approx 0.95$ , whereas the value predicted using the Rankine-Hugoniot relations and the muzzle exit velocity is  $\approx 2.9$ .

### 4.3 RESULTS FROM LASER-INDUCED INCANDESCENCE

Measurements of the laser-induced incandescence intensity can also yield additional information about the flow field. Because the optical system was calibrated with a spectral radiance standard, it could be determined that the spectral radiance observed as a result of laser-heated particulates would be generated by a blackbody at 1,266 K. If it is assumed that carbon particulates in the size range 0.01 to 1.0  $\mu\text{m}$  and at a temperature of 1,266 K occupy the viewing volume, then the particulate number density range is  $3.4 \times 10^8 - 3.4 \times 10^{12} \text{ cm}^{-3}$ .

Using the relative intensity of the incandescence at 1,000  $\mu\text{sec}$  measured at 5,976 and 8,284  $\text{\AA}$  and the Planck blackbody relation, a particulate temperature of 1,280 K was calculated. This is in excellent agreement with the temperature value obtained using the spectral radiance calibration.

Considering only conduction heat losses from the particulates, an estimate of particulate heating by the laser beam can be made using the method outlined by Eckbreth (Ref. 17). The relation used by Eckbreth was

$$T_p = T_{pi} + \frac{\alpha q a}{4k_a} \quad (10)$$

in which  $T_p$  is the final particulate temperature,  $q$  is the laser flux,  $k_a$  is the heat conductivity of the propellant gas flow regime,  $a$  is the particulate radius, and  $\alpha$  is the overall particulate absorption coefficient.  $T_{pi}$  is the initial particulate temperature, and it was assumed to be 757 K (the predicted value of temperature at 1,000  $\mu\text{sec}$ .). An air heat conductivity value of  $1.18 \times 10^{-4} \text{ cal/sec} \cdot \text{cm} \cdot \text{K}$  for a temperature of 757 K was obtained from Kreith (Ref. 19). The laser flux was taken to be  $5.2 \times 10^4 \text{ watts/cm}^2$ . On the assumption that  $\alpha = 0.9$  and  $a = 0.2 \mu\text{m}$ , the particulate temperature was calculated to be 1,229 K, which is consistent with previous particulate temperature values.

### 5.0 SUMMARY

The muzzle blast flow field presents a complex, hostile environment for nonintrusive diagnostic techniques. The short duration of the flow (6 msec) presents a difficult requirement for temporal resolution of the measurement technique and the timing sequences of the data acquisition system. The laser-Raman system used in the experiments reported



herein successfully solved these electronic, optical, and mechanical problems. Because of laser-induced particulate incandescence, the primary objective of resolving the actual gas temperature in the muzzle blast region was not achieved. However, the secondary objectives of verifying applicability of laser Raman diagnostics to short pulse expansions and providing beneficial muzzle blast information were accomplished. A number of more detailed conclusions regarding these experiments are listed below.

1. Particulates (probably carbon) on the order of  $0.4\text{-}\mu\text{m}$  diameter and with a concentration of  $\approx 10^8/\text{cc}$  exist near the muzzle exit plane at  $t > 600\ \mu\text{sec}$ . Laser transmission measurements indicate that the particle concentration is much higher for  $0 < t < 600\ \mu\text{sec}$ ; therefore, laser scattering diagnostics of any type in this temporal region would be suspect because of multiple scattering effects.
2. A laser power density of  $5 \times 10^4\ \text{watts}/\text{cm}^2$  heated the particulates to  $1,250\ \text{K}$ , and the resulting incandescence was of higher intensity than the Raman signals to be used for temperature and number density measurements. Because of the large shot-to-shot variations in incandescence level, the primary objective of these experiments (static temperature measurement) could not be met.
3. Measurements of  $\text{N}_2$  and  $\text{CO}$  number densities were successfully made for  $t > 600\ \mu\text{sec}$  and for  $t < 0$  by using multiple cannon firings and subtracting out off-band incandescence contributions to the on-band Raman measurements. The temporal resolution of the measurements was  $60\ \mu\text{sec}$ . Predicted values of temperature had to be assumed to reduce the data, and the estimated data uncertainty is 25 to 30 percent. Values of  $n(\text{N}_2)/n_\infty$  measured in the precursor flow are approximately a factor of three below predicted values.
4. Based on the agreement of the measured  $n(\text{N}_2)/n_\infty$  values with predictions assuming  $T_e = 1,000\ \text{K}$  and an isentropic expansion, the inability to detect an  $\text{N}_2$  vibration-rotation anti-Stokes signal, and the laser beam particulate heating calculation using the predicted temperature value as the initial particulate temperature, it is concluded that the temperature near the exit plane of the muzzle is  $\leq 1,000\ \text{K}$ .

## REFERENCES

1. Schmidt, E. M. and Shear, D. D. "Formation and Decay of Impulsive, Supersonic Jets." AIAA Paper No. 74-531, presented at the AIAA 7th Fluid and Plasma Dynamics Conference, Palo Alto, California, June 17-19, 1974.
2. Schmidt, E. M. and Shear, D. D. "Optical Measurements of Muzzle Blast." *AIAA Journal*, Vol. 13, No. 8, August 1975, pp. 1086-1091.
3. Schmidt, E. M., Gion, E. J., and Shear, D. D. "Acoustic Thermometric Measurements of Propellant Gas Temperatures in Guns." *AIAA Journal*, Vol. 15, No. 2, February 1977, pp. 222-226.
4. Schmidt, E. M., Fansler, K. S., and Shear, D. D. "Trajectory Perturbations of Fin-Stabilized Projectiles Due to Muzzle Blast." *Journal of Spacecraft and Rockets*, Vol. 14, No. 6, June 1977, pp. 339-344.
5. Erdos, J. I. and Del Guidice, P. D. "Calculation of Muzzle Blast Flowfields." *AIAA Journal*, Vol. 13, No. 8, August 1975, pp. 1048-1055.
6. Freeman, R. A. "Variable-Energy Blast Waves." *British Journal of Applied Physics*, Series 2, Vol. 1, 1968, pp. 1697-1710.
7. Bauer, P. G. and Frankle, J. M. "The Simulation of Interior Ballistic Performance of Guns by Digital Computer Program." BRL-R-1183, Ballistic Research Laboratories, Aberdeen Proving Ground, Maryland, December 1962.
8. Celmins, A. K. R. "Theoretical Basis of the Recoiless Rifle Interior Ballistics Code 'RECRIF'." BRL-R-1931, Ballistic Research Laboratories, Aberdeen Proving Ground, Maryland, September 1976.
9. Klingenberg, G. and Mach, H. "Experimental Study of Non-Steady Phenomena Associated with the Combustion of Solid Gun Propellants." *Sixteenth Symposium (International) on Combustion*, The Combustion Institute, Pittsburgh, Pennsylvania, 1977.
10. Oswatitsch, K. "Intermediate Ballistic." FSTC 381-T65-372 (AD473249), December 1964. (Translated from Deutsche Luft-und Raumfahrt FB 64-37, December 1964.) Deutschen Versuchsanstalt fur Luft-und Raumfahrt, Aachen, Germany.

11. Placzek, G. "The Rayleigh and Raman Scattering." Translated from a publication of the Akademische Verlagsgesellschaft G.m.b.H., Leipzig, 1934, *Handbuch der Radiologie*, Heft 6, Teil 2, pp. 209-374.
12. Placzek, G. and Teller, E. "Die Rotationsstruktur der Ramanbanden Mehratomiger Molekule." *Zeitschrift fur Physik*, Vol. 31, March 1933.
13. Sushchinskii, M. M. *Raman Spectra of Molecules and Crystals*. Israel Program for Scientific Translations, New York, 1972.
14. Anderson, A., Ed. *The Raman Effect, Vol. 2: Applications*. Marcel Dekker, Inc., New York, 1973.
15. Williams, W. D. and Lewis, J.W.L. "Rotational Temperature and Number Density Measurements of N<sub>2</sub>, O<sub>2</sub>, CO, and CO<sub>2</sub> in a Hypersonic Flow Field Using Laser-Raman Spectroscopy." AEDC-TR-75-37 (ADA012877), July 1975.
16. Drake, M. C. and Rosenblatt, G. M. "Rotational Raman Scattering from Premixed and Diffusion Flames." *Combustion and Flame*, Vol. 33, No. 2, 1978, pp. 179-196.
17. Eckbreth, A. C. "Effects of Laser-Modulated Particulate Incandescence on Raman Scattering Diagnostics." *Journal of Applied Physics*, Vol. 48, No. 11, November 1977, pp. 4473-4479
18. Cohen, A., Kleiman, M., and Cooney, J. "Lidar Measurements of Rotational Raman and Double Scattering." *Applied Optics*, Vol. 17, No. 12, 15 June 1978, pp. 1905-1910.
19. Kreith, F. *Principles of Heat Transfer*. International Textbook Co., Scranton, Pennsylvania, 1963.

## NOMENCLATURE

a	Nominal radius of particulates in the flow field, $\mu\text{m}$ or cm
$C_{FR}$	Relative sensitivity of detection system at the two wavelengths monitored in the rotational structure
$C_{FV}$	Relative sensitivity of detection system at the two wavelengths monitored in a vibration-rotation band
$C_F(T,X)$	Temperature-dependent correction factor for determining species X number density
$C_F(X)$	Calibration factor for determining species X number density
c	Speed of light, cm/sec
DTR	Diaphragm test room
h	Planck's constant
$I(X,Q_0)$	Intensity of the Species X, $v = 0$ , Q-branch
$I_s(\lambda)$	Relative spectral sensitivity of the optical system at wavelength $\lambda$ as determined by a standard lamp calibration
$k_a$	Thermal conductivity of air
$M_e$	Mach number at muzzle exit
$n(X)$	Number density of species, X
$n_e$	Total number density of species at muzzle exit
$n_\infty$	Ambient total number density
$p_e$	Static pressure at the muzzle exit
$p_\infty$	Ambient static pressure
q	Laser flux at viewing volume
$R_R$	Measured intensity ratio in the rotational structure
$R_s$	Ratio of the relative system sensitivities at two wavelengths

$R_v$	Measured intensity ratio in the vibration-rotation band
$R_\sigma$	Ratio of $N_2$ vibration-rotation band scattering cross section to that of CO
T	Temperature
$T_e, T_\infty$	Temperature at muzzle exit; ambient temperature
$T_{pi}, T_p$	Initial particulate temperature prior to laser heating; final particulate temperature
t	Time
$u_m$	Muzzle exit velocity, m/sec
v	Vibrational level quantum number
X	Indicates a molecular species, either CO or $N_2$
$\alpha$	Overall absorption coefficient of particle at the laser wavelength
$\lambda$	Wavelength
$\nu_o$	Frequency of laser radiation
$\sigma(X,Q)$	Scattering cross section of species X, vibration-rotation band Q-branch

**SUBSCRIPTS**

c	Indicates a calculated value
m	Indicates a measured value

**SUPERSCRIPTS**

o	Indicates atmospheric calibration conditions
t	Indicates muzzle blast flow-field conditions